



HAL
open science

Highly evolved miaskitic syenites deciphering the origin and nature of enriched mantle source of ultrapotassic magmatism in the Variscan orogenic root (Bohemian Massif, Moldanubian Zone)

Martin Kubeš, Jaromír Leichmann, David Buriánek, Markéta Holá, Petr Navrátil, Stéphane Scaillet, Paul O'Sullivan

► To cite this version:

Martin Kubeš, Jaromír Leichmann, David Buriánek, Markéta Holá, Petr Navrátil, et al.. Highly evolved miaskitic syenites deciphering the origin and nature of enriched mantle source of ultrapotassic magmatism in the Variscan orogenic root (Bohemian Massif, Moldanubian Zone). *Lithos*, 2022, 432-433, pp.106890. 10.1016/j.lithos.2022.106890 . insu-03795335

HAL Id: insu-03795335

<https://insu.hal.science/insu-03795335>

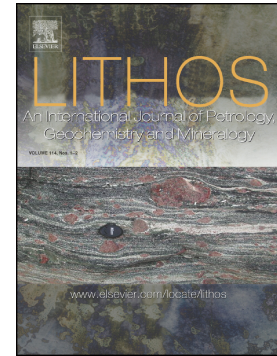
Submitted on 4 Oct 2022

HAL is a multi-disciplinary open access archive for the deposit and dissemination of scientific research documents, whether they are published or not. The documents may come from teaching and research institutions in France or abroad, or from public or private research centers.

L'archive ouverte pluridisciplinaire **HAL**, est destinée au dépôt et à la diffusion de documents scientifiques de niveau recherche, publiés ou non, émanant des établissements d'enseignement et de recherche français ou étrangers, des laboratoires publics ou privés.

Journal Pre-proof

Highly evolved miaskitic syenites deciphering the origin and nature of enriched mantle source of ultrapotassic magmatism in the Variscan orogenic root (Bohemian Massif, Moldanubian Zone)



Martin Kubeš, Jaromír Leichmann, David Buriánek, Markéta Holá, Petr Navrátil, Stéphane Scaillet, Paul O'Sullivan

PII: S0024-4937(22)00299-7

DOI: <https://doi.org/10.1016/j.lithos.2022.106890>

Reference: LITHOS 106890

To appear in: *LITHOS*

Received date: 9 June 2022

Revised date: 19 September 2022

Accepted date: 24 September 2022

Please cite this article as: M. Kubeš, J. Leichmann, D. Buriánek, et al., Highly evolved miaskitic syenites deciphering the origin and nature of enriched mantle source of ultrapotassic magmatism in the Variscan orogenic root (Bohemian Massif, Moldanubian Zone), *LITHOS* (2022), <https://doi.org/10.1016/j.lithos.2022.106890>

This is a PDF file of an article that has undergone enhancements after acceptance, such as the addition of a cover page and metadata, and formatting for readability, but it is not yet the definitive version of record. This version will undergo additional copyediting, typesetting and review before it is published in its final form, but we are providing this version to give early visibility of the article. Please note that, during the production process, errors may be discovered which could affect the content, and all legal disclaimers that apply to the journal pertain.

Highly evolved miaskitic syenites deciphering the origin and nature of enriched mantle source of ultrapotassic magmatism in the Variscan orogenic root (Bohemian Massif, Moldanubian Zone)

Martin Kubeš^{a,b,*}, Jaromír Leichmann^a, David Buriánek^{a,b}, Markéta Holá^c, Petr Navrátil^d, Stéphane Scaillet^e, Paul O'Sullivan^f

^a Department of Geological Sciences, Masaryk University, Kotlářská 2, 602 00, Brno, Czech Republic

^b Czech Geological Survey, Klárov 3, 118 21, Praha, Czech Republic

^c Department of Chemistry, Masaryk University, Kamenice 753/5, 602 00, Brno, Czech Republic

^d Diamo S. E., Branch GEAM, 592 51 Dolní Rožínka, Czech Republic

^e CNRS/INSU, BRGM, Université d'Orléans, ISTO, UMR 7327, 45071, Orléans, France

^f GeoSep Services, Pine Cone Road 1521, Moscow, 83843, Idaho, USA

* Corresponding author

E-mail address: kubes@mail.muni.cz

Abstract

A detailed study of alkali-rich syenites from the Gföhl unit of the Moldanubian Zone in the Bohemian Massif provides constraints on the exact origin and character of mantle source of ultrapotassic magmatism in the Variscan orogenic root in Central Europe. The syenites are characterized by highly alkaline composition (K_2O 11.3–12.7 wt%; K_2O/Na_2O 6.8–7.5), crust-like isotopic signatures ($^{87}Sr/^{86}Sr_{335} \sim 0.7116$; $\epsilon Nd_{335} \leq -7.8$), and significant trace element enrichment (Th, U, Zr, Hf, LILE, LREE). They host an extraordinary amount of zircon (0.5–5 vol%) along with subordinate titanite and apatite, reflecting their miaskitic affinity. Mineral chemistry suggests that syenites formed through fractional crystallization and accumulation from highly reduced,

metaluminous to slightly peraluminous mantle-derived alkaline magmas. Whole-rock geochemistry and Sr-Nd isotopes provide direct evidence that they were produced by partial melting of metasomatic phlogopite-bearing vein network (glimmerites) in the lithospheric mantle, generated by the interaction of (U)HP fluids/melts derived from deeply subducted crustal material (Moldanubian granulites) with wall-rock peridotites. Low-degree partial melting of pure vein component produced unusual geochemical signatures of miaskitic syenites, compared to the composition of common ultrapotassic rocks in the Bohemian Massif, reflecting relatively higher degrees of partial melting of mixed glimmerite-peridotite mantle source.

The emplacement of alkali-rich syenites was almost contemporaneous with the mantle source enrichment and closely followed by initial fast cooling dated by $^{40}\text{Ar}/^{39}\text{Ar}$ amphibole-biotite ages ranging between 329.8 ± 1.6 and 331.4 ± 0.7 Ma, corresponding to rapid exhumation of the Variscan orogenic root in Central Europe. The U-Pb apatite age of 305.2 ± 5.3 Ma likely reflects further cooling to lower temperatures. The syenite emplacement was linked to the early impulse of ultrapotassic magmatism associated with the Andean-type subduction of the Saxothuringian domain beneath the Moldanubian block. The close temporal association of K-rich magmatism in the Saxothuringian and Moldanubian Zone is indicated by identical cooling ages of miaskitic syenites and other Saxonian ultrapotassic rocks, as revealed by $^{40}\text{Ar}/^{39}\text{Ar}$ dates around 330 Ma.

Keywords: (ultra)potassic magmatism, mantle metasomatism, phlogopite-rich source, low-degree melting, Bohemian Massif

1. Introduction

Mantle-derived potassic to ultrapotassic magmatism, typically related to post-collision extensional settings, represent magmatic proxy to trace lithospheric processes and thus allow to study effects of crustal recycling in subduction zones. The ultrapotassic magmas in orogenic belts are usually characterized by high K_2O and MgO contents (Foley, 1992), elevated $\text{K}_2\text{O}/\text{Na}_2\text{O}$ ratios, enrichment in large ion lithophile elements (LILE) and light rare earth elements (LREE), and continental crust-like isotopic signatures (e.g. Altherr et al., 2004; Conticelli et al., 2009; Zhao et al.,

2009). It is widely accepted that such geochemical and isotopic composition of K-rich magmas is generated by partial melting of lithospheric mantle domains previously modified by modal metasomatism (e.g. Conticelli et al., 2015; Prelević et al., 2012). Metasomatic assemblages of hydrous minerals, commonly forming vein networks entrapped within wall-rock mantle peridotite (Foley et al., 2013), can be reactivated during later melting events, caused by a regional extension (Foley, 1992). Therefore, ultrapotassic magmatic activity typically accompanies high and ultra-high pressure (HP/UHP) metamorphism (Janoušek and Holub, 2007) within deeper levels of subduction zones, as demonstrates occurrences of alkaline K-Mg-rich rocks in many collisional belts, involving Variscan and Alpine Orogen in Europe (e.g. Ersoy and Palmer, 2013; von Raumer et al., 2014).

The internal orogenic domain of the Variscan belt in the Bohemian Massif (Fig. 1a) hosts diverse types of ultrapotassic rocks (Janoušek et al., 2019, 2020, Krmíček et al., 2016; Kubínová et al., 2017) and hence provide a unique insight into geodynamic and magmatic evolution of deeper parts of the Variscan Orogen during subduction-related events. The deep Variscan burial of crustal assemblages is recorded by a close spatial association of HP felsic granulites with garnet-bearing ultrabasic rocks (Kubeš et al., 2022) along with the presence of UHP phases preserved in host granulites (Kotková et al., 2011; Perraki and Farayad, 2014).

This study focuses on mineralogical, geochemical, and isotopic characteristics of alkali-rich miaskitic syenites, combined with conventional geochronological dating, in order to shed light on the petrogenesis and magmatic evolution of the highly evolved member of post-collision K-rich magmatism in the Moldanubian Zone (Bohemian Massif). The syenites geochemically correspond to miaskitic rocks, however, their genesis differs from common miaskitic varieties, since they originated through accumulation of mantle-derived alkali-rich magmas without significant prolonged subsequent differentiation processes at shallow crustal levels (see Marks and Markl, 2017 for review). Importantly, the major element composition and extreme trace element enrichment of the alkali-rich syenites along with their crust-like Sr isotopic signatures identify an exact origin and nature of enriched mantle source for (ultra)potassic magmas in the Bohemian Massif, corresponding to phlogopite-bearing vein network enclosed in the subcontinental lithospheric mantle. Furthermore, our geochemical data indicate that the alkali-rich syenites represent initial melts produced by a low-degree

melting of phlogopite-dominated component, whereas other ultrapotassic members (e.g. durbachites, lamproites, lamprophyres) reflect relatively higher degrees of partial melting of rather mixed peridotite-phlogopite material.

2. Geological settings

The studied intrusion of the alkali-rich syenites is situated southeast of the ultrapotassic Třebíč pluton (Fig. 1b) belonging to the so-called durbachite series of the eastern Moldanubian Zone – the high-grade root of the Variscan Orogen in the Bohemian Massif (Janoušek et al., 2020; Janoušek and Holub, 2007). The internal orogenic domain mostly consists of medium- to high-grade metamorphic rocks extensively intruded by numerous granitoid plutons (Žák et al., 2014).

The Moldanubian Zone is traditionally subdivided into three principal tectonostratigraphic units differing in lithological assemblages and metamorphic conditions: the Monotonous, Varied and Gföhl units (e.g. Lardeaux et al., 2014). Mid-crustal, amphibolite-facies Monotonous and Varied units, generally termed Drosendorf unit, mainly consist of garnet-sillimanite paragneisses along with subordinate orthogneisses and amphibolites. Neoproterozoic-Early Paleozoic sedimentation ages were determined for the protolith of both mid-crustal complexes (Košler et al., 2014). The lower crustal Gföhl unit is composed of anatectic orthogneisses and migmatites, and amphibolites accompanied by HP granulites (Tajčmarová et al., 2006). The HP felsic granulites usually enclose spinel and/or garnet-bearing peridotites hosting pyroxenite and eclogite layers (Kubeš et al., 2022; Medaris et al., 2005). The magmatic protolith of the Gföhl gneisses shows Cambrian-Devonian ages (Friedl et al., 2004).

The Variscan metamorphic evolution of the Moldanubian Zone was accompanied by extensive plutonic activity taking place in contrasting geodynamic settings, mostly from Late Devonian to Carboniferous (Žák, et al. 2014; references therein). These various igneous stages include: (1) calc-alkaline and high-K calc-alkaline subduction-related suites of the Central Bohemian Plutonic Complex (~373–340 Ma); (2) (ultra)potassic, Mg-rich plutons of the durbachite series, associated with rapid exhumation of the Gföhl unit to mid-crustal assemblages (~340–355 Ma); (3) peraluminous anatectic

S-type and high-K, I-type granitoids (~330–326 Ma) followed by (4) small calc-alkaline intrusions with I-type affinity of the Moldanubian Plutonic Complex (~320–300 Ma).

The vigorous (ultra)potassic magmatism of the Moldanubian Zone, a characteristic feature of the entire European Variscan belt (von Raumer et al., 2014), is documented by widespread occurrence of durbachitic plutons which form two NNE–SSW oriented belts within the Bohemian Massif (see Janoušek and Holub, 2007 for review). Most plutons of the Eastern Durbachite Belt, involving large and smaller satellite bodies on Czech (Třebíč, Jihlava, Drahonín) and Austria territory (Rastenberg, Ybbs), have been previously investigated in detail from a geochemical, geochronological or geophysical approach (e.g. Gerdes et al., 2000; Janoušek et al., 2013, 2020; Kotková et al., 2010; Leichmann et al., 2017). By contrast, the relatively small intrusion of alkali-rich syenites studied here has remarkable geochemical composition and uncertain origin (Leichmann et al., 2004) that has been the focus of only a few petrological/mineralogical studies so far (Kubeš et al., 2021; Leichmann et al., 1998, 2004; Škoda et al., 2009). The syenites have attracted attention especially because of their significantly high radioactivity (U ~390 ppm, Th ~700 ppm; Leichmann et al., 1998) dictated by extreme high field strength elements (HFSE) enrichment (e.g., ZrO₂ up to 2.3 wt%; Leichmann et al., 2004) due to extraordinary amount of zircon (up to 5 vol%; Škoda et al., 2009) and its extensive late hydrothermal alteration (Kubeš et al., 2021).

3. Sampling and analytical methods

The relatively small intrusion of the alkali-rich syenites (up to 100 m long) from the Gföhl unit of the Moldanubian Zone was systematically sampled in order to cover all differentiated syenite varieties (Fig. 2a–c) (10 samples for each variety), described in Section 4.1. Consequently, the samples were processed to polished thin sections for detailed optical microscopy studies (Fig. 2d, e) and subsequent analytical techniques described below.

Zircon crystals were separated by crushing and sieving of the central syenite variety to a fraction of 64–512 µm and subsequently were concentrated by magnetic and liquid (tetrabromomethane) separation. Secondary electron (SEM) images, showing zircon morphology (Fig.

3a), were taken by a JEOL 6490 LV scanning electron microscope using an accelerating voltage of 15 kV and beam current of 1 nA. Back-scattered electron (BSE) images (Fig. 3b–f) along with major and minor element chemistry of rock-forming and accessory phases (Table 1, 2), were obtained with a Cameca SX 100 electron microprobe (EMP). Operating conditions for individual spot analyses were as follows: wavelength-dispersive mode, an accelerating voltage of 15 kV, a beam current of 10 nA, and a beam size of 2 μm for common accessory minerals (zircon, titanite, ilmenite), 5 μm for silicates (feldspars, amphibole, biotite, chlorite), and 10 μm for apatite. The following natural and synthetic standards were used: sanidine (Si, Al), orthoclase (K), baryte (Ba), albite (Na), wollastonite (Ca), pyrope (Mg), hematite (Fe), titanite (Ti), vanadinite (Cl, V, Pb), zircon (Zr), ThO_2 (Th), topaz (F), fluorapatite (P).

Trace elements concentrations of major accessory phases (Table 3) were measured by laser ablation-inductively coupled plasma-mass spectrometry (LA-ICP-MS). The instrumentation consisted of LSX-213 G2+ laser ablation device and Agilent 7900 ICP-MS analyser with an octopole reaction cell. The laser operates at a wavelength of 213 nm with a pulse duration ≤ 4 ns. Using helium as a carrier gas with a flow rate of 0.9 l min^{-1} . The aerosol was mixed with argon serving as makeup gas with flow rate 1 l min^{-1} and transported to the ICP-MS. The mass spectrometer operated at the forward power of 1550 W and Ar gas flow rate of 15 l min^{-1} (outer plasma gas). Ablation spot was from 40 to 50 μm in diameter, regarding the area analyzed. Repetition rate was 10 Hz and fluence 5 J cm^{-2} . One spot was analyzed for 60 s. Total integration time was 4.1 s. External calibration was performed using the standard reference materials (SRM) NIST 610 and NIST 612. Quantification was based on the sum of oxides. The total sum of all oxides (estimated from the elemental analysis by LA-ICP-MS) was normalized to 100 wt%. Then the analytes were expressed as elements in ppm. This method is internal standard independent and does not require the precise determination of the reference element by another analytical method at the specific area of the ablation spot. If the sample contains water or another component non-determinable by LA-ICP-MS (e.g. fluorine, hydrogen...), the normalization has to be performed to the sum obtained by subtracting the content of this component from 100 wt% (determined by another method or known from the general mineral formula).

The whole-rock major element composition (Table 4) was determined in the AcmeLabs Vancouver (Bureau Veritas) by ICP-OES after fusion with lithium borate flux. Trace elements, including rare earth elements (REE), were analyzed using ICP-MS with additional lithium tetraborate fusion. In addition, incompatible transition metals (Cr, Ni, V, Sc) were determined by ICP-MS after modified aqua regia digestion. For more analytical details, reproducibility, and detection limits see <https://www.acmelab.com>. Whole-rock Sr-Nd isotopic analyses were performed at Activation Laboratories Ltd., (ActLabs) Ontario. Sample dissolution in HF:HNO₃ and chemical separation procedures for Sr and Nd follow the methodology of Creaser et al. (2004). Isotope analyses were performed using a VG354 5-collector machine in a multi-dynamic data collection mod. Accuracy of the Sr and Nd isotopic composition was monitored using the NIST SRM987 and JNdi-1 isotopic standards. The long-term measured values of these standards were as follows: $^{87}\text{Sr}/^{86}\text{Sr} = 0.710269 \pm 21$ (1 σ , n = 50) and $^{143}\text{Nd}/^{144}\text{Nd} = 0.512096 \pm 11$ (1 σ , n = 11). For further analytical information see <https://www.actlabs.com>.

The U-Pb apatite dating (Table 5) along with mineral separation were performed at GeoSep Services (GSS) laboratory, Idaho. Apatite grains were separated from the original sample material using standard procedures combined with specific customized procedures described by Donelick et al. (2005). Laser spot locations were selected using optical microscope Zeiss Axioplan with transmitted light at 2000x magnification, which allowed for the recognition of features below the surface of individual grains. An Agilent 7700x quadrupole ICP-MS equipped with a New Wave Nd-YAG 213 nm laser ablation system was used to acquire the U-Pb isotopic ratios. For all laser analyses, the beam diameter was 20 μm and the frequency was set at 5 Hz, yielding ablation pits 16–18 μm deep. Ultra-high purity He and Ar gas were used to deliver the ablated material into the plasma source. The isotopes measured included ^{43}Ca , ^{147}Sm , ^{204}Pb , ^{206}Pb , ^{207}Pb , ^{232}Th , and ^{238}U (45 scans over 45 sec). Approximately 20 seconds were allowed between each analysis in order to clear the system prior to the next background data collection. Standards used included the Duluth complex FC, McClure Mountain MM, and Durango DR, which encompasses a wide standard age range from 1099 to 31.44 Ma (see Weber et al., 2019 for further analytical information).

$^{40}\text{Ar}/^{39}\text{Ar}$ dating experiments were conducted on single biotite and amphibole grains (Table 6) extracted by gently crushing the samples. Loose grains were ultrasonically bathed in deionized water and rinsed until no suspension was released, then dried in a vented oven at 50 °C and inspected under a high-magnification binocular. The single grains were irradiated together for 10 h along with the neutron flux standard sanidine FCs (28.305 ± 0.036 Ma; Renne et al., 2010) in the dedicated Cd-lined CLICIT neutron flux facility at TRIGA-Corvallis (OR, USA). The data were regressed and corrected for instrumental parameters (blank, mass discrimination, SEM dead-time, post irradiation decay, and atmospheric contamination, J -gradient monitoring). Typical blanks (n fA) were 3×10^{-2} (m/e = 36), 3×10^{-2} (m/e = 37), 7×10^{-3} (m/e = 38), 4×10^{-2} (m/e = 39), 4×10^{-1} (m/e = 40). Individual and pooled age errors are quoted at $\pm 1\sigma$ and include propagation of all instrumental and procedural uncertainties. Plateau ages (PA) are calculated as the inverse-variance weighted mean of contiguous steps featuring a figure of merit (Mean Squared Weighted Deviation, MSWD) falling in the fiducial interval. Total-gas ages (TGA) are calculated by individually summing the Ar isotopes of all fractions and by linearly propagating the associated errors (equivalent to a standard K/Ar age).

4. Results

4.1. Petrography

The petrography of the alkali-rich syenites has been previously described by Leichmann et al. (1998) and Kubeš et al. (2021), and thus only a brief petrographic description of samples used in this study are given here. The investigated syenite intrusion is exposed on the slopes of the Oslava river valley (two outcrops up to 100 m long) situated ca. 4 km northwest of the city Náměšť and Oslavou (Czech Republic), nearby the largest durbachitic body (Třebíč pluton) (Fig. 1b) in the Bohemian Massif (Janoušek et al., 2020). The syenites intrude high-grade crustal assemblages of the Gföhl unit mainly consisting of migmatized gneisses and biotite-bearing migmatites. Both outcrops of alkali-rich syenites are separated from ultrapotassic rocks of the Třebíč pluton by a several hundred meters wide zone of amphibole–biotite gneisses and biotite migmatites. The syenite intrusion consists of three

texturally, mineralogically and petrographically different syenite varieties (Fig. 2a–c), designated in this study as follows: (1) central (2) marginal (3) nodule variety. The classification of individual syenite varieties is based on the combination of both spatial (central–marginal) and textural (nodule) features.

The central variety is built up by fine-grained, orange to red-colored leucocratic rock (Fig. 2a) with a gradual transition to more melanocratic marginal variety. K-feldspar represents the dominant rock-forming mineral (up to 92 vol%) reaching the highest modal amount in central variety. It usually forms subhedral grains of relatively small size (~0.4 cm) compared to K-feldspar from marginal and nodule varieties (up to 1.5 cm). Very fine inclusions containing iron oxide are most likely responsible for its orange to red colour, a typical feature observed within all described syenite varieties (Fig. 2a–c). Subhedral to euhedral amphibole is regularly dispersed in the rock (<5 vol%) and exhibits a relatively high intensity of chloritization, which ordinarily progresses along cleavage plains of amphibole. A characteristic feature of the leucocratic variety is unusually high modal abundances of metamict zircon (~5 vol%) commonly surrounded by abundant microfractures (Fig. 2d). Quartz and plagioclase are typically absent. Tabular grains of biotite are completely replaced by chlorite (<1 vol%). Accessory phases commonly occur as U-thorite, titanite, apatite and ilmenite. Rare relicts of strongly altered thorianite and cheralite were observed exclusively within the central variety (Kubeš et al., 2021).

The marginal variety is characterized by medium- to coarse-grained texture, orange colour, lower K-feldspar abundances (7–82 vol%) and relatively high modal amount of amphibole (up to 10 vol%) and biotite (~1.8 vol%) regularly dispersed in the host rock (Fig. 2b). The prevailing K-feldspar usually occurs as subhedral grains with relatively variable sizes (0.6–1.5 cm). The green, pleochroic, sub- to euhedral amphibole grains (Fig. 2e) are locally replaced by secondary chlorite along cleavage plains. In contrast to central variety, zircon amount (0.5 vol%) considerably decreases in marginal variety. Moreover, amount of quartz (~3.5 vol%) and partially chloritized biotite moderately increases in marginal variety relative to central variety. Plagioclase is ordinarily absent or occurs in rare cases as strongly altered relicts. Its alteration products are white mica, albite, and scapolite–marialite. Accessory phases usually include titanite, apatite, U-thorite and ilmenite.

The nodule variety was described based on amphibole grains clustering into small nodules (up to 5 cm across) within the medium- to coarse-grained marginal variety (Fig. 2c). Such characteristic feature of nodule variety reflects its high modal amount of amphibole reaching up to 17 vol%. Accordingly, K-feldspar amount is lower (77 vol%) and zircon amount slightly increases (~0.8 vol%) in the nodule variety compared to marginal variety. Plagioclase is mostly absent, whereas quartz (~2.5 vol%) and chloritized biotite (~2 vol%) amount is similar to marginal variety. Accessory phases are titanite, apatite, U-thorite and ilmenite.

4.2. Mineral textures and chemistry (EMP)

4.2.1. Feldspars

The subhedral perthitic K-feldspar ($\text{Or}_{36.4-6.7}$) the most wide-spread rock-forming phase in syenites, exhibits quite uniform chemistry among described varieties (Table 1), with K_2O and BaO content varying between 14.2–16.3 wt% and 0.33–0.64 wt%, respectively. Plagioclase is ordinarily absent or rarely occurs as elongated inclusions (<0.3 mm) in the K-feldspar and/or irregular aggregates (0.5 mm) within the K-feldspar rim. Both forms mainly consist of sodic plagioclase ($\text{An}_{1.8-7.6}$) with similar chemistry.

4.2.2. Mafic phases

The sub- to euhedral amphibole dominates from mafic silicates and corresponds to Fe-rich pargasite ($\text{Fe}/(\text{Fe}+\text{Mg}) = 0.74-0.91$; $^{\text{A}}(\text{Na}+\text{K})$ up to 0.89 apfu) (Fig. 4a). Amphibole is commonly intergrown with chloritized biotite or gradually replaced by secondary chlorite along its cleavage planes. It has slightly higher total alkali contents ($\text{Na}+\text{K} \sim 0.77-0.89$ apfu) and lower Mg# (0.09–0.17; $\text{Mg\#} = \text{molar Mg}/[\text{Mg} + \text{FeO}_{\text{tot}}]$) in marginal and nodule variety compared to central variety ($\text{Na}+\text{K} \sim 0.61-0.81$ apfu; $\text{Mg\#} 0.21-0.26$). Note that amphibole in nodule variety and amphibole from direct

contact between central and marginal variety plot in the middle of the fractionation trend shown in Mg# vs. Al diagram (Fig. 4b).

Fresh biotite occurs as tabular grains (<280 μm) enclosed in perthitic K-feldspar and/or closely associated with amphibole. Biotite corresponds to annite ($\text{Fe}/(\text{Fe}+\text{Mg}) = 0.82\text{--}0.92$) with the lowest Mg# values in marginal variety similar to amphibole (Table 1). Biotite is usually replaced by secondary chlorite of chamosite-like composition ($\text{Fe}/(\text{Fe}+\text{Mg}) = 0.72\text{--}0.83$) without significant chemical variations among syenite varieties. Besides, chlorite occurs as extremely fine-grained alteration products of titanite.

4.2.3. Zircon

Zircon usually forms euhedral crystals ranging from 100 to 350 μm in size. They have dominantly well-developed pyramids (101) and prisms (100) (Fig. 3a), less frequently evolved pyramids (121), (211), (301), and prism (110). Early magmatic inclusions in zircon typically consist of U-thorite (Fig. 3b). The vast majority of zircon experienced self-induced structural radiation damage (metamictization), followed by recrystallization (Fig. 3b) and/or fluid-driven hydrothermal alteration (Fig. 3c).

We present only EMP data from unaltered partially recrystallized zircon since the post-magmatic alteration extensively affected zircon chemistry, as exemplified by enhanced contents of non-formula elements (e.g. Ca, Fe, Al, P) and low ZrO_2 content, EMP analytical totals, and BSE intensity (Fig. 3c) (see Kubeš et al., 2021 for details). Pristine zircon (Fig. 3d) has relatively high ZrO_2 (~64–66 wt%) and SiO_2 (~32–33 wt%) contents, and low Th/U ratios (<1.5) with non-formula element contents below EMP detection limits (Table 2). Concentrations of UO_2 (0–1.6 wt%) and ThO_2 (0–1.3 wt%) vary widely on the inter- and intra-grain scale. Zircon from central variety shows slightly decreased HfO_2 content (0.98–1.23 wt%) and thus higher Zr/Hf ratios (~52–67) in contrast to marginal and nodule variety (HfO_2 1.07–1.96 wt%; Zr/Hf ~32–55).

4.2.4. U-thorite

U-thorite occurs as irregular to rounded relatively small inclusions (<15 μm) enclosed in metamict zircon (Fig. 3b). The chemistry of early magmatic inclusions from only unaltered zircon domains are presented within this section (Table 3). The pristine U-thorite usually exhibit high ThO_2 (43.9–56.5 wt%) and UO_2 (19.3–30.0 wt%) contents, accompanied by variable ZrO_2 concentrations (0.14–4.32 wt%) routinely below 1 wt%, together with high EMP analytical totals (99–101.6 wt%).

4.2.5. Titanite

Titanite in all described syenite varieties exhibits somewhat distinct textural morphologies, mineralogical associations, and zonation patterns. Titanite mainly occurs as sub- to euhedral grains varying from 100 to 700 μm in size, intergrown with amphibole and/or closely associated with ilmenite. It also forms euhedral diamond-shaped crystals (<350 μm) enclosed in K-feldspar, often displaying patchy zonation patterns. In some cases, well-developed subhedral to euhedral crystals have preserved original oscillatory and/or sectorial zonation (Fig. 3e). Similar to zircon, titanite crystals experienced late fluid-driven alteration resulting in partial replacement of titanite by secondary anatase, reflected by high TiO_2 content and low EMP analytical totals and BSE intensities of extensively altered titanite domains (see Kubeš et al., 2021 for details). Therefore, chemical composition of pristine titanite is reported in this study (Table 2).

Unaltered titanite has a uniform chemical composition (TiO_2 36–38 wt%, SiO_2 30–31 wt%, CaO ~29 wt%) among individual syenite varieties and distinct textural types. It contains relatively high concentrations of Nb_2O_5 reaching up to 0.32 wt% (Table 2). Most titanite crystals show somewhat high $\text{Ti}^{4+}/(\text{Al} + \text{Fe}^{3+})$ ratios commonly ranging between 8.3–16.2.

4.2.6. Apatite

Apatite is typically present as sub- to euhedral short-prismatic crystals about maximum sizes of 250 μm and/or forms rounded grains reaching up comparable sizes (~200 μm). Apatite is usually

enclosed in perthitic K-feldspar and/or closely associated with amphibole. Apatite displays no visible effects of late alteration in contrast to zircon and titanite. The oscillatory magmatic zoning of apatite grains is commonly preserved (Fig. 3f).

It chemically corresponds to fluorapatite (F ~3.40–3.85 wt%). Concentrations of P₂O₅ and CaO are similar among syenite varieties and vary between 40.7–43 wt% and 55–56 wt%, respectively. Apatite shows uniform and relatively high MnO and SiO₂ contents in described varieties, reaching up to 0.13 wt% and 0.67 wt% (Table 2).

4.2.7. Ilmenite

Ilmenite occurs as irregular grains in the form of small inclusions within amphibole cleavage plains (<10 μm), larger intergrowths with titanite (650–900 μm), and subhedral crystals enclosed in K-feldspar (250–500 μm). Ilmenite has uniform chemical composition (TiO₂ ~52 wt%, FeO ~46 wt%) with Nb₂O₅ content routinely varying between 0.12–0.3 wt% (Table 2).

4.3. Trace elements in minerals (LA-ICP-MS)

4.3.1. Zircon

With respect to the presence of abundant early magmatic U-thorite inclusions in zircon (Fig. 3b), we provide data obtained for inclusion-free grains and/or domains of pristine zircon (Fig. 3d), in line with time-resolved LA-ICP-MS spectra. The partially recrystallized zircon domains with no visible effects of alteration display considerably variable Σ REE, Y, Th, and U contents, within and between syenite varieties, regularly varying from several hundred up to tens of thousands of ppm (Table 3).

Chondrite-normalized REE patterns (McDonough and Sun, 1995) differ among individual varieties (Fig. 5a). Zircon in central variety typically features heavy rare earth elements (HREE)-enriched patterns ($Sm_N/Yb_N < 0.13$) with negative Eu anomalies ($Eu_N/Eu_N^* 0.46–0.71$; $Eu_N^* = \sqrt{(Gd_N \times$

Sm_N) and more pronounced LREE enrichment relative to zircon in other syenite varieties (Fig. 5a). Zircon in marginal variety has relatively flat REE patterns, slightly enriched in HREE (Sm_N/Yb_N 0.36–1.29), with strong negative Eu anomalies ($\text{Eu}_N/\text{Eu}_N^*$ 0.28–0.55), similar to zircon from nodule variety (Sm_N/Yb_N 0.17–1.58; $\text{Eu}_N/\text{Eu}_N^*$ 0.35–0.59).

4.3.2. Titanite

Titanite hosts significant amounts of incompatible trace elements such as REE + Y and HFSE, particularly Nb and Ta (Table 3). Titanite is characterized by substantially variable $\sum\text{REE}$ abundances within and between individual varieties, reaching up the highest contents in marginal variety (up to 6477 ppm) in contrast to titanite from central (1748–5027 ppm) and nodule variety (<960 ppm). Yttrium exhibits similar decreases from marginal (30–1364 ppm) through central (37–475 ppm) to nodule variety (46–273 ppm). Niobium and Ta show a relatively uniform distribution in titanite among syenite varieties, varying between 356–1124 ppm and 39–195 ppm, respectively. Other HFSE such as Th, U, and Zr reach up somewhat lower contents ranging from tens to several hundreds of ppm (Table 3), occasionally Zr content rises to thousands of ppm. Titanite usually has low Th/U ratios (0.5–2.9) and Ga concentrations (<23 ppm).

Chondrite-normalized REE patterns of titanite ordinarily feature convex-upward trends (Ce_N/Yb_N up to 21.7) with considerably variable Eu anomalies, involving well-marked positive ($\text{Eu}_N/\text{Eu}_N^*$ 1.98–7.01) as well as strong negative Eu anomalies ($\text{Eu}_N/\text{Eu}_N^*$ 0.37–0.74) even within syenite variety itself, as demonstrated by titanite chemistry from marginal variety (Fig. 5b). It should be noted that $\sum\text{REE} + \text{Y}$ contents rapidly decreases with the increasing magnitude of positive Eu anomaly (Fig. 5b).

4.3.3. Apatite

Apatite contains rather low HFSE contents compared to zircon and titanite although it commonly reaches up relatively significant amounts of REE and Sr (Table 3). Apatite from central

variety exhibits the highest $\sum\text{REE}$ (1634–4188 ppm) and Y (630–1560 ppm) contents in contrast to apatite from marginal variety ($\sum\text{REE}$ 1811–3285 ppm, Y 238–397 ppm) that shows values similar to those from nodule variety ($\sum\text{REE}$ 1684–3269 ppm, Y 161–496 ppm). Concentrations of Sr are lower in apatite from the central variety (132–196 ppm) compared to apatite in marginal (257–311 ppm) and nodule variety (218–297 ppm).

Chondrite-normalized REE patterns of apatite display slight variations among syenite varieties (Fig. 5c). Apatite from central variety features relatively flat REE patterns (Ce_N/Yb_N 1.8–2.6) caused by enrichment in HREE (Lu_N 279–755). By contrast, apatite in marginal and nodule variety has more pronounced convex-upward REE patterns reflected by higher Ce_N/Yb_N (6.0–20.7) due to lower HREE contents (Lu_N 50–164). Apatite shows deep negative Eu anomalies without any significant variations among described syenite varieties ($\text{Eu}_N/\text{Eu}_N^*$ 0.25–0.71).

4.4. Whole-rock geochemistry

4.4.1. Major and minor elements

The alkali-rich syenites are generally characterized by significantly high K_2O content (up to 12.7 wt%) and $\text{K}_2\text{O}/\text{Na}_2\text{O}$ ratio (6.8–7.6) along with moderately high SiO_2 (up to 64 wt%) and Al_2O_3 (~17 wt%), and low MgC (≤ 47 wt%), CaO (≤ 1.62 wt%), TiO_2 (≤ 0.82 wt%), P_2O_5 (≤ 0.08 wt%) contents. Syenites have considerably low Mg# (≤ 0.17) and show somewhat variable FeO_{tot} (0.9–5.07 wt%), reaching the highest contents in nodule and marginal variety, similar to MgO, CaO, TiO_2 , and P_2O_5 concentrations (Table 4). Total alkali content (particularly K_2O) and SiO_2 gradually increases from nodule through marginal to central variety (Fig. 6a). Due to pronounced K_2O enrichment, all syenite varieties fall in the shoshonitic field (Fig. 6b) within the SiO_2 vs. K_2O diagram (Peccerillo and Taylor, 1976). The central variety is slightly peraluminous (A/CNK 1.01–1.05; molar $\text{Al}_2\text{O}_3/[\text{CaO} + \text{K}_2\text{O} + \text{Na}_2\text{O}]$), whereas marginal and nodule variety display a rather metaluminous character (A/CNK 0.94–0.99; Fig. 6c) (Shand, 1943). By contrast, peralkalinity slightly decreases from marginal and nodule variety (A/NK up to 1.10–1.12; molar $\text{Al}_2\text{O}_3/[\text{K}_2\text{O} + \text{Na}_2\text{O}]$) to central variety (A/NK 1.06–

1.08). The K-rich syenites are highly ferriferous and geochemically resemble quartz syenite composition within the multicationic plot B vs. $Mg/(Fe + Mg)$ (Fig. 6d) (Debon and Le Fort, 1988), illustrating a relationship between maficity and $Mg\#$ values.

4.4.2. Trace elements

The syenites exhibit various enrichment in total REE contents, with a decreasing trend from central through nodule to marginal variety (ΣREE 177–270 ppm, 128–212 ppm, 84–96 ppm, respectively). Chondrite-normalized REE patterns slightly differ among individual varieties (Fig. 7a). Marginal and nodule variety are characterized by convex-upward REE patterns (Ce_N/Yb_N 2.85–8.84) with more pronounced negative Eu anomaly typical for nodule variety (Eu_N/Eu_N^* 0.53–0.87) relative to marginal variety (Eu_N/Eu_N^* 0.79–0.96). By contrast, central variety displays LREE- and HREE-enriched U-shaped patterns with pronounced MREE depletion (Fig. 7a), featuring weak or no negative Eu anomaly (Eu_N/Eu_N^* 0.85–1.00).

Primitive mantle-normalized (McDonough and Sun, 1995) extended trace element patterns show strong HFSE (Zr, Th, U, Hf) and LILE (Cs, Rb, Ba, K, Pb) enrichment and significant Nb and Ti depletion along with deep troughs for P (Fig. 7b). All syenite varieties have notably low concentrations of transition metals (Cr 3.1–5.4 ppm, Ni 0.7–1.7, Sc 6–26 ppm). High LILE/HFSE, Th/Ta, Rb/Sr and low K/Rb and Rb/Cs ratios represent a typical signature of syenites.

4.5. Sr-Nd isotopic composition

Strontium and neodymium isotope data were recalculated for the precise (CA-ID-TIMS) U–Pb zircon age of 335.127 ± 0.061 Ma obtained for the Třebíč pluton (Schaltegger et al., 2021), corresponding to contemporaneous emplacement of alkaline (ultra)potassic intrusions in the Gföhl unit (Fig. 1b; see Section 5.5. for details). Whole-rock Sr-Nd isotope geochemistry of central and marginal variety (Fig. 8a; Table 4) of the alkali-rich syenites is characterized by highly radiogenic $^{87}Sr/^{86}Sr_{335}$ (~ 0.7116), similar to those of potassic to ultrapotassic magmas of durbachitic and lamproite series

within the Moldanubian Zone of the Bohemian Massif (see Janoušek et al., 2019, 2020; Krmíček et al., 2016 for review). Moreover, unradiogenic Nd of syenite samples ($\epsilon\text{Nd}_{335} \leq -7.8$), along with Sr isotopic signatures, strikingly resemble those of mature continental crust (Fig. 8a).

4.6. Geochronology

4.6.1. U-Pb apatite dating

As stated above, apatite has not experienced extensive dissolution during the post-magmatic hydrothermal alteration in contrast to titanite and metamict zircon (Kubeš et al., 2021), and thus represents an ideal phase for dating of (post-)magmatic history of syenites. Overall, twenty-six apatite crystals from marginal variety were analyzed (Table 5). Contents of U and Th in dated apatite grains regularly vary between 4.7–157.3 ppm and 5.7–322.0 ppm, with U/Th values of 0.31–1.07 (median 0.63). Twenty-six spots yield a well-defined isochron date of 305.9 ± 5.3 Ma (MSWD of 2.2; Fig. 9), corresponding to a cooling age of miaskitic syenites.

4.6.2. $^{40}\text{Ar}/^{39}\text{Ar}$ dating of mafic silicates

The age spectra of amphibole and biotite reveal variable $^{40}\text{Ar}/^{39}\text{Ar}$ degassing patterns among the samples (Fig. 10a, b). Amphibole 4NL yielded a first, highly discordant, spectrum featuring a prominent hump over the first 80 % of ^{39}Ar released and culminating near 320 Ma at 40 % of cumulative loss (run N319.MS3; Fig. 10a). The trend ends with a final (fusion) step at 329.8 ± 1.6 Ma. The age trend is paralleled by large and progressively declining $^{36}\text{Ar}/^{39}\text{Ar}$ ratios early through the gas release, indicating progressive exhaustion of a secondary atmospheric component in the course of the experiment (and most probably associated to degassing of secondary intergrown biotite). A duplicate run on another single crystal produced a much more regular spectrum with a concordant plateau spanning more than 80 % of the total release at 329.4 ± 0.7 Ma (run N320.MS3; Fig. 10a). Biotite 3GN (run N317.MS3; Fig. 10b) shows initially constant apparent ages clustering about a short plateau

segment at 332.1 ± 0.7 Ma (35 % of initial ^{39}Ar released) before evolving into an erratic pattern featuring consecutive deeps (down to 100 Ma) as the extraction proceeds. Conversely, biotite 2AM (run N318.MS3; Fig. 10b) produced a discordant (though less irregular) pattern converging to a short plateau segment at 331.4 ± 0.7 Ma (1σ) in the last 25 % of ^{39}Ar released.

All in all, the different experiments appear to have isolated a common radiogenic component near 330 Ma (Table 6) despite sample-specific irregularities due to secondary alteration to chlorite, both in amphibole and biotite. The near-concordance of the biotite and amphibole data at 330.9 ± 0.39 Ma (pooled mean of four preferred ages noted above) is significant and gives robustness to this estimate with a MSWD score of 2.84 (i.e., just above the fiducial limit of 2.60 at the 95 % confidence interval). The concordance is all the more so compelling given the distinctive retention behavior characterizing these phases (McDougall and Harrison, 1999), clearly pointing to a cooling of the syenite intrusion below ca. 500 °C close to 330 Ma.

5. Discussion

5.1. Mineral assemblages unraveling magmatic evolution of syenites

The alkali-rich syenites host a significant amount of HFSE-bearing phases dominated by zircon along with subordinate titanite and apatite, reflecting their miaskitic affinity. Although the syenites mineralogically and geochemically correspond to miaskitic magmas, they genetically differ from common miaskitic varieties, considering their formation through the accumulation of alkali-rich melts (see below) without subsequent extensive differentiation stage of mafic and/or ultramafic assemblages (e.g. nephelinites, basanites, alkali basaltic rocks) that are typically associated with miaskitic rocks (Marks and Markl, 2017; references therein). The accessory minerals together with major rock-forming phases provide a unique insight into the (post-)magmatic history of the syenites and shed light on their mutual petrogenetic relation with the host rocks.

The miaskitic syenites originated by crystal accumulation mechanism rather than crystallization from residual melt, for the following reasons. Zircon from central variety has lower HfO_2 content and

higher Zr/Hf ratio relative to zircon from marginal variety (Table 2), reflecting a degree of magma fractionation (Hoskin and Schaltegger, 2003). Since zircon is generally considered as an early magmatic phase, the extreme ZrO₂ saturation of the central variety (ZrO₂ up to 2.6 wt%; Table 4) triggered the crystallization of accumulated zircon pockets prior to zircon crystallization in marginal parts of the syenite intrusion. Likewise, higher total alkali content and decreased Mg# of amphibole from marginal variety (Fig. 4a, b; Table 1) demonstrate that amphibole crystallized from more evolved melt. Considering variations in the amphibole chemistry among syenite varieties, best illustrated by the fractionation trend in the Mg# vs. Al diagram (Fig. 4b), nodule variety likely represents a transitional member between central and marginal variety and emphasizes the importance of crystal accumulation. The above-mentioned observations are further supported by different whole-rock trace-element composition of syenite varieties. Significant HREE and HFSE (Zr, Hf, Th, U) enrichment in central variety reflects zircon accumulation (Fig. 7b; Table 4). The nodule variety ordinarily shows intermediate contents of trace elements compared to central and marginal varieties (Fig. 7b), indicating its transitional character. By contrast, the lowest trace element concentrations typical of marginal variety suggest possible AFC-style crustal contamination (see Section 5.2.).

The magmatic origin of zircon is documented by low Th/U ratios (Hoskin and Schaltegger, 2003) and its morphological features (Fig. 3a) resembling those of high-temperature igneous zircons associated with mantle-derived alkaline magmas (Škoda et al., 2009). LREE-enriched zircon patterns (Fig. 5a), usually ascribed to occurrences of micro- to submicroscopic inclusions (Zhong et al., 2018; references therein), likely reflect the variable intensity of metamictization and/or recrystallization (see Kubeš et al., 2021 for details), indicating that zircon chemistry cannot be considered as a suitable petrogenetic tracer to decipher the magmatic evolution of the host rocks.

Trace element signatures of titanite correspond to those from igneous rocks worldwide (e.g. Kontonikas-Charos et al., 2019), considering relatively high Σ REE and HFSE contents (Table 3) and convex-upward REE patterns (Fig. 5b), mimicking the whole-rock composition (Fig. 7a). Conversely, positive Eu anomalies and variable Σ REE + Y contents relate to a late metasomatic overprint of syenites (Kubeš et al., 2021), as suggested by negative Eu anomalies on whole-rock and apatite REE patterns (Fig. 5c, 7a) along with Σ REE + Y decrease in titanite depending on the magnitude of

positive Eu anomaly (Fig. 5b). By contrast, relatively high $Ti^{4+}/(Al + Fe^{3+})$ ratios of pristine titanite (up to 16.2) can indicate a mantle-related magma source (Piuzana et al., 2008). Low Fe_2O_3/Al_2O_3 ratios and Ga contents in unaltered titanite and its preserved negative Eu anomalies (Fig. 5b; Table 3) likely reflect reduction state of the parental magma, since under reducing conditions divalent cations such as Fe^{2+} , Ga^{2+} , and Eu^{2+} are not favored by titanite, leading to their low contents (Xu et al., 2015). This is in agreement with petrological observations such as the presence of abundant ilmenite and the absence of allanite, whose formation requires high Fe^{3+} proportions in magmas (Sha and Chappell, 1999).

In contrast to other HFSE-bearing phases, igneous fluorapatite shows no visible effects of later alteration and thus represent a suitable petrogenetic tracer. The increase in HREE and Y with decreasing Sr contents in apatite from central to marginal variety (Fig. 5c; Table 3) reflects geochemistry of host magma, particularly increased aluminosity accompanied by higher SiO_2 contents (Fig. 6c; Table 4) (e.g. Chu et al., 2009). Relatively high MnO contents in apatite (Table 2), resembling those from highly fractionated metaluminous to slightly peraluminous granitoids (Belousova et al., 2002), indicate increasing aluminosity and/or reducing conditions (Sha and Chappell, 1999). Taken together, trace element systematics in apatite is highly sensitive to increasing aluminosity and SiO_2 content of the host rocks rather than a degree of magma fractionation, which in turn is reflected by zircon and amphibole chemistry, as discussed above.

5.2. Ultrapotassic affinity versus the role of AFC-style crustal contamination

Although the miaskitic syenites are of cumulate origin, the considerably high K_2O content and K_2O/Na_2O ratio (Table 4), extreme enrichment in HFSE (Th, U, Zr, Hf) and LILE (Cs, Rb, Ba, Pb) (Fig. 7b), and crust-like isotopic signatures (Fig. 8a) indicate their alkaline, ultrapotassic affinity (e.g. Altherr et al., 2004; Conticelli et al., 2015; Foley et al., 1992). High LILE/HFSE, Th/Ta, Rb/Sr as well as low K/Rb and Rb/Cs ratios are generally considered as a characteristic fingerprint of ultrapotassic rocks of the durbachite series (Janoušek and Holub, 2007). Primitive mantle-normalized trace element patterns also suggest a genetic link to ultrapotassic magmatism in the Bohemian Massif (Fig. 7b), as

further indicated by a close spatial association of the alkali-rich syenites with the Třebíč pluton (Fig. 1b). Moreover, the syenites share some geochemical and isotopic features with Group II lamprophyres from Vosges and Schwarzwald (Soder and Romer, 2018), indicating a similar magma source (Section 5.3.).

On the other hand, the highly ferriferous character of the syenites (Fig. 6d), significantly low contents of transition metals (Table 4) and the composition of Fe-rich mafic silicates (Fig. 4) point towards the AFC-style crustal contamination of source magmas of the alkali-rich syenites, as previously proposed for other syenitoids in the Moldanubian Zone (Janoušek et al., 2019). In addition, the presence of quartz and biotite xenocrysts exclusively in marginal and nodule variety indicates assimilation of felsic crustal material during magma ascent (Kubínová et al., 2017). However, the highly unusual major- and trace-element whole-rock fingerprints of miaskitic syenites (extremely high Ba, K, Rb, Th, U, Zr; Fig. 7b; Table 4) cannot be simply ascribed to the hybridization of syenite parental melts by mature crustal material since contents of these elements in the syenites are by far higher than those of crustal continental rocks and sediments (e.g. Rudnick and Fountain, 1995). Thus, unreasonably high proportions of crustal assimilants would be required to generate LILE- and HFSE-rich melts of miaskitic composition (Zhang et al., 2009). Accordingly, the alkali-rich syenites show a different geochemical trend in the A/CNK vs. A/NK diagram (Fig. 6c) compared to strongly contaminated marginal facies of the Třebíč pluton, usually exhibiting notably low K₂O, Rb, Ba, Th, and U contents (Janoušek et al., 2020). From this follows that extreme K₂O, LILE and HFSE (Th, U, Zr, Hf) enrichment makes the syenites almost entirely insensitive to crustal contamination and provide constraints on the source nature and concurrently its degree of melting (Section 5.4.).

Similarly, crust-like isotopic signatures of the syenites ($^{87}\text{Sr}/^{86}\text{Sr}_{335} \sim 0.7116$; $\epsilon\text{Nd}_{335} \leq -7.8$) could not have been produced solely by continental crustal assimilation (Fig. 8b), instead the involvement of a long-term enriched reservoir is necessary to generate such highly radiogenic isotopic composition (Gerdes et al., 2000; Tabaud et al., 2015). Furthermore, as already shown for durbachitic rocks of the Třebíč pluton (Janoušek et al., 2020), likely crustal assimilants are isotopically less evolved ($^{87}\text{Sr}/^{86}\text{Sr}_{337} \leq 0.7102$; $\epsilon\text{Nd}_{337} > -6.5$) than the ultrapotassic primary magma ($^{87}\text{Sr}/^{86}\text{Sr}_{337} \geq 0.7112$; $\epsilon\text{Nd}_{337} > -7.6$). These observations unequivocally preclude the contribution of crustal

contamination as a major mechanism producing the typical crust-like isotopic composition of the syenites, indicating negligible and/or only limited dilution of source isotopic signatures (Fig. 8b).

Trace element modelling confirms that low degree (~1 %) melting of a phlogopite-bearing mantle source (see Section 5.4. for details) would generate appropriate parental melt compositions. We use the batch melting model of Shaw (1970) for the starting composition glimmerite (Förster et al. 2017) and for mineral/melt partition coefficients, we use the values reported in Condamine et al. (2022). The most obvious difference between the modeled melt composition and the studied miaskitic syenites is that the proposed parental melt have higher LREE, Sr and Nb (Fig. 7c). The content of Nb in the melt produced by partial melting of the mantle is strongly affected by the presence of rutile in melting residue (Altherr et al., 2004) which is not incorporated in our model. High contents of these elements reflect LREE and Sr enrichment in the source coupled with small degrees of melting. These differences indicate that the parental melts were during emplacement partially modified by fractionation and assimilation of crustal material (Fig. 7c, 8c, d).

Results from AFC modelling (Bohlen and Spera, 2001) confirm that the assimilation of anatectic melts into fractionated magma can explain the composition of studied rocks (Fig. 7c, 8b–d). The mineral composition requires low degree crystal fractionation (3–5 %) of a parental magma in combination with anatectic melt generated by partial melting of the Moldanubian crust (5GB/9; Buriánek 2008). The depletion in Sr and an insignificant negative Eu anomaly suggest that plagioclase (~60 %) and biotite (~35 %) remained the main crystallizing phase during magma evolution. However, the assumed presence of accessory phases strongly controls the modelled HFSE and REE contents. The crystallization of monazite (1 %; monazite group minerals are typical accessory minerals in durbachites of the Třebíč pluton; Buriánek et al. 2022), apatite (0.5 %), and allanite (0.5 %) depleted modelled melt composition mainly in LREE. In addition, variations in the content of accessory phases (e.g. titanite/apatite ratio) can affect REE content in individual samples (Fig. 8d).

5.3. Origin and nature of enriched mantle source

General agreement exists that highly alkaline ultrapotassic magmatism relates to the melting of heterogeneous lithospheric mantle source contaminated by crustal material (e.g. Avanzinelli et al., 2009; Conticelli et al., 2015; Foley, 1992; Jung et al., 2020; Prelević et al., 2012). The significant contribution of mature continental crust to the source region of miaskitic syenites is demonstrated by crust-like isotopic signatures (Fig. 8a), HFSE (Zr, Th, U, Hf) and LILE enrichment (Fig. 7b), and slight negative Eu anomalies (Fig. 7a; Table 4). Depletions in Nb, Ta and Ti suggest the presence of Ti-rich phase in their melting residue (Altherr et al., 2004), a typical feature observed in convergent tectonic settings (e.g. Zhao et al., 2009), signaling that the input of crustal component was probably subduction-related. Peralkaline composition of syenites along with significantly high K_2O content and K_2O/Na_2O ratio (Table 4), exceeding those of lamproite series (Fig. 6b) (Krmíček et al., 2016), suggest a predominance of K-rich phase within their source, most likely phlogopite (Soder and Romer, 2018). LREE-enriched patterns with negative Eu anomalies of marginal and nodule variety, showing no visible effects of crystal accumulation in contrast to central variety (Fig. 7a), possibly indicate partial melting in the presence of residual phlogopite (Kubínová et al., 2017). High Rb/Sr, Ba/Rb, and low Ti/K ratios, admittedly at least partially modified by cumulus processes, may also suggest derivation of syenites from a phlogopite-bearing mantle source (Jung et al., 2020).

Indeed, a key role of phlogopite within the enriched mantle source of ultrapotassic rocks worldwide has been previously demonstrated by many authors (e.g. Conticelli et al., 2015; Prelević et al., 2008; Zhao et al., 2009). However, the exact origin and nature of the mantle source of ultrapotassic magmatism in the Bohemian Massif remain unclear. Basically, two possible alternatives have been proposed by Janoušek et al. (2020): (1) phlogopite-bearing harzburgitic mantle, and/or (2) phlogopite-veined refractory peridotite. With respect to the results of experimental studies (Förster et al., 2019; references therein), the extreme K_2O -enrichment of syenites (up to 12.7 wt%) provide direct evidence that highly evolved miaskitic melts were derived from almost pure phlogopite component concentrated within a vein network. Since experimentally produced melts of uniform phlogopite-bearing peridotite exhibit relatively limited K_2O enrichment (<4 wt% K_2O ; Condamine et al., 2016). Instead, partial melting of phlogopite-veined refractory peridotite has successfully generated such extremely K-rich melts (K_2O up to 12 wt%; Förster et al., 2017).

Accordingly, K-rich syenites together with durbachitic rocks of the Třebíč pluton (Janoušek et al., 2020) have Sr-Nd isotopic compositions similar to Moldanubian HP granulites and phlogopite-rich veins collectively termed as glimmerites (Fig. 8a) (Becker et al., 1999) that could account for a major source of ultrapotassic magmatism in the Bohemian Massif, as demonstrated above. These glimmerite veins, occurring within ultrabasic massifs in the Moldanubian Zone of Lower Austria, formed through the interaction of wall-rock peridotites with F-rich fluid released during the HP–HT breakdown of phlogopite in the felsic granulites (Becker et al., 1999). The supercritical fluids and/or possibly (U)HP melts derived from subducted felsic metaigneous lithologies (Janoušek et al., 2004), have percolated through overlaying heterogeneous subcontinental mantle, which has led to the formation of phlogopite-rich vein network. There is mounting evidence that Moldanubian granulites have truly reached mantle depths, as demonstrated by the spatial association with mantle-derived ultrabasic rocks (Kubeš et al., 2022), preservation of UHP phases in granulites (Kotková et al., 2011; Perraki and Faryad, 2014), and PT estimates of their prograde mineral assemblages (Jedlička et al., 2015). Moreover, HP granulites are spatially and temporally associated with ultrapotassic rocks of the durbachite series and share mutual chemical affinities (Janoušek and Holub, 2007).

A similar petrogenetic scenario was previously proposed for durbachites and Group II lamprophyres from the Vosges and Schwarzwald (Soder and Romer, 2018; Tabaud et al., 2015). The notable geochemical and isotopic similarities between the lamprophyres and the alkali-rich syenites, involving almost identical REE patterns and Sr-Nd isotopic composition resembling those of Moldanubian granulites (Fig. 7a, 8; see Soder and Romer, 2018), indicate comparable mantle source enrichment. However, partial melting of higher proportions of glimmerite component would be required to produce the unusual major and trace element composition of the syenites (Fig. 7c; see Section 5.4.). From this follows that our whole-rock geochemical data demonstrate a derivation of the alkali-rich syenites from a pure vein system consisting of phlogopite-bearing assemblages resembling glimmerites.

5.4. Low-degree partial melting of phlogopite-veined mantle domains

The conspicuous variable enriched composition of miaskitic syenites compared to closely associated ultrapotassic rocks of the Třebíč pluton is suggestive of heterogeneous lithospheric mantle source and particularly a different degree of its partial melting. Assuming that the metasomatic component is concentrated within the vein network, a low degree of partial melting of pure glimmerite material would produce the K-rich melts with extreme trace element enrichment (Fig. 7b, c; Table 4) (Förster et al., 2017, 2019), as demonstrated in case of (ultra)potassic rocks from the Mediterranean region (Conticelli et al., 2009) and Lhasa terrane (Zhao et al., 2009). Taking into account the results of experimental studies investigating melting of mixed peridotite-glimmerite mantle source (Förster et al., 2017), metasomatic assemblages of vein network usually have a lower solidus than surrounding refractory lithospheric mantle. Hence with increasing temperature, during a short thermal pulse likely caused by slab break-off (Janoušek et al., 2020), the phlogopite-veined mantle domains should preferentially partially melt, whereas partial melting of main rock peridotite would occur only if the temperature has sufficiently raised. Accordingly, a sufficient heat flux of the invading asthenosphere would trigger partial melting of the phlogopite-bearing metasomatized mantle, producing (ultra)potassic magmas (e.g. Avanzinelli et al., 2009; Becker et al., 1999; Prelević et al., 2008).

These observations together with our trace element-based partial melting models (Fig. 7c) clearly indicate that the alkali-rich syenites represent an initial product of low-degree melting of metasomatically enriched subcontinental lithospheric mantle beneath the Variscan orogenic root. By contrast, the origin of common members of ultrapotassic magmatism in the Moldanubian Zone of the Bohemian Massif is linked to relatively higher degrees of partial melting of the similar metasomatized source (Janoušek and Holub, 2007; Krmíček et al., 2016; Kubínová et al., 2017), inevitably increasing the contribution of a lithospheric mantle component to the hybrid vein-derived magmas (Janoušek et al., 2020). In this context, extreme HFSE and LILE enrichment along with unusually high K_2O content of miaskitic syenites (Fig. 6b, 7b; Table 4) indicate the dominant contribution of the pure metasomatic component to their parental magmas, with almost negligible input of mixed peridotite-glimmerite source. Since trace element enrichment in partial melting products of the phlogopite-veined depleted mantle are strongly dependent on temperature and therefore on a degree of melting (Fig. 7c); the highest enrichment generally reflects the lowest degree of melting, as was experimentally

demonstrated by Förster et al. (2017). Accordingly, low-degree melting of K-rich mantle domains with non-peridotitic mineral assemblages may produce small-volume partial melts with unique geochemical characteristics (e.g. Foley, 1992), providing a possible explanation for low Mg# of the syenites along with negligible Cr, Ni and V contents (Table 4). Since glimmerites represent unusual mantle rocks with crust-like geochemical and isotopic signatures inherited from their precursors (Moldanubian granulites; Becker et al., 1999), the initial melts (alkali-rich syenites) would be dominated by vein components, whereas later melts (ultrapotassic rocks; Janoušek et al., 2020) will include components from the peridotitic wall rocks.

An analogous vein-plus-wall-rock melting model was applied to lamproitic magmatism in the Western Mediterranean region (Conticelli et al., 2009), where variable geochemical and isotopic composition between lamproites and less evolved calc-alkaline to shoshonitic members were attributed to different degrees of partial melting of lherzolitic mantle along with different proportions of phlogopite and clinopyroxene entering these melts.

5.5. Timing of K-rich magmatism in the Variscan orogenic root

The newly acquired U-Pb apatite age of 305.9 ± 5.3 Ma in the current study (Fig. 9) corresponds to the cooling of the miaskitic syenites instead of their emplacement, considering a higher temperature of crystallization of alkaline ultrapotassic melts (>800 °C; Kotková et al., 2010) relative to the U-Pb closure temperature of apatite (~ 375 – 570 °C; Cochrane et al., 2014). Accordingly, the almost contemporaneous emplacement of highly alkaline ultrapotassic rocks in the Moldanubian Zone of the Bohemian Massif is recorded by U-Pb zircon, titanite, and rutile ages in a range of 335–338 Ma obtained for durbachitic plutons (Janoušek et al., 2020; Kotková et al., 2010; Schaltegger et al., 2021), subordinate two-pyroxene syenitoids (Janoušek et al., 2019) and vaugnerite and syenite porphyry from an ultrapotassic dyke swarm (Kubínová et al., 2017). These coeval intrusions reflect the first pulse of ultrapotassic magmatism in the Variscan orogenic belt (Soder and Romer, 2018), near-synchronous and shortly following the exhumation of (U)HP crustal complexes (Janoušek and Holub, 2007).

The initial fast cooling of the alkali-rich syenites recorded by new $^{40}\text{Ar}/^{39}\text{Ar}$ amphibole-biotite dates ranging between 329.8 ± 1.6 and 331.4 ± 0.7 Ma (Fig. 10a, b; Table 6) indicates that exhumation of the internal orogenic domain in the Bohemian Massif must have been a short-lived event, probably driven by buoyancy forces (Medaris et al., 2005), as suggested by relatively narrow time gap between the peak stage of high-grade Variscan metamorphism (~340 Ma; O'Brien and Rötzler, 2003) and cooling ages of the mantle-derived alkaline syenites. The rapid exhumation of the Variscan orogenic root in Central Europe, accompanying the ultrapotassic magma emplacement (Leichmann et al., 2007), is further supported by: (1) $^{40}\text{Ar}/^{39}\text{Ar}$ dating of units overridden by the Gföhl nappes (Dallmeyer et al., 1992); (2) cooling rates given for mantle-derived rocks (Medaris et al., 2005); (3) presence of granulite clasts in the Culmian foreland basin (Čopjaková et al., 2005).

5.6. Possible geodynamic implications

Our results also shed light on possible geodynamic settings of the emerging subduction channel between Moldanubian and Saxothuringian domains during the Variscan collision (Schulmann et al., 2014; references therein). Whole-rock geochemical and isotope data indicate that miaskitic syenites originated by partial melting of pure glimmerite component veining mantle wedge (Section 5.3.), derived from Moldanubian granulites (Becker et al., 1999). Assuming that HP granulites represent a deeply buried Saxothuringian felsic metaigneous material (Janoušek et al., 2004), relatively short-lived Andean-type subduction (Late Devonian–Early Carboniferous) appears to be a most likely geodynamic scenario (Schulmann et al., 2009). During subduction of Saxothuringian domain underneath the eastern continental Teplá-Barrandian-Moldanubian block, a local lithospheric mantle could have been extensively affected by melts/fluids derived from the down-going slab material. The mantle enrichment leading to glimmerite veins formation dated at 337 Ma (Becker et al., 1999) was almost contemporaneous with K-rich magmas emplacement (~335 Ma; e.g. Schaltegger et al., 2021). Such widespread mantle refertilization is probably recorded by the presence of K-rich melt inclusions trapped in Saxonian eclogites from Granulitgebirge (Borghini et al., 2020), exhibiting chemical features typical of common durbachitic rocks (Janoušek et al., 2020). Accordingly, occurrences of

genetically related yet widely separated lithospheric mantle fragments in the Moldanubian and Saxothuringian Zone (Schmädicke et al., 2010) may suggest a similar mantle source of ultrapotassic rocks in both major tectonic zones of the Bohemian Massif.

After the formation of phlogopite-rich vein network within the subcontinental lithospheric mantle, a sudden heat pulse was necessary to reactivate these subduction-derived metasomatic assemblages (Janoušek et al., 2020). In our case, buoyancy forces following slab break-off (Medaris et al., 2005) likely triggered low-degree partial melting of glimmerite-veined mantle producing highly alkaline miaskitic and ultrapotassic melts (Foley, 1992; Avanzine'li et al., 2009; Conticelli et al., 2015). The subsequent passage of these melts through continental blocks, accompanied by extensive crustal assimilation (Janoušek et al., 2020), has caused only limited dilution of their initial geochemical and isotopic signatures (Fig. 7c, 8b–d) during magma ascent to shallow crustal levels (ca. 8–15 km; Leichmann et al., 2017). The relatively slow solidification rate of these hot dry magmas and/or possibly their slow ascent through the crust (Krková et al., 2010) is reflected by the U-Pb cooling age of apatite (Fig. 9) following the initial fast cooling of miaskitic syenites below ca. 500 °C (McDougall and Harrison, 1999) recorded by $^{40}\text{Ar}/^{39}\text{Ar}$ dates (Fig. 10a, b). Our $^{40}\text{Ar}/^{39}\text{Ar}$ ages are nearly identical to the cooling ages of other ultrapotassic members from the Saxothuringian Zone (e.g. Meissen massif; see Wenzel et al., 1997), highlighting the close temporal yet wide spatial association of mantle-derived K-rich magmatism within the European Variscides.

6. Conclusions

The studied alkali-rich syenites, located in the high-grade Gföhl unit of the Moldanubian Zone, represent a “missing puzzle piece” to decipher the exact origin and nature of enriched mantle source of ultrapotassic magmatism in the Bohemian Massif. The syenites are characterized by having a highly alkaline composition ($\text{K}_2\text{O} \leq 12.7$ wt%; $\text{K}_2\text{O}/\text{Na}_2\text{O} \leq 7.5$), miaskitic affinity, radiogenic Sr and unradiogenic Nd isotopes ($^{87}\text{Sr}/^{86}\text{Sr}_{335} \sim 0.7116$; $\epsilon\text{Nd}_{335} \leq -7.8$), and significant trace element enrichment (e.g. Th, U, Zr, Hf, LILE, LREE). They originated as a result of fractional crystallization and accumulation from highly evolved mantle-derived alkaline magmas. Their extreme major and

trace element geochemistry along with crust-like isotopic signatures bear witness that syenites correspond to products of partial melting of metasomatic phlogopite-rich vein network (glimmerites) in the subcontinental mantle, generated by the percolation of (U)HP fluids/melts released from the deeply subducted continental crust (Moldanubian granulites) during the Variscan collision. Low-degree melting of high proportions of almost pure phlogopite component produced unusual miaskitic melts, compared to common members of ultrapotassic magmatism in the Bohemian Massif (e.g. durbachites, lamprophyres, lamproites), linked to higher degrees of partial melting of mixed glimmerite-peridotite mantle source. The almost contemporaneous emplacement of alkaline magmas with mantle source enrichment was closely followed by initial fast cooling dated by $^{40}\text{Ar}/^{39}\text{Ar}$ amphibole-biotite ages (≤ 331.4 Ma), indicating rapid exhumation of the high-grade root of the Variscan Orogen, whereas U-Pb apatite age of 305.9 Ma rather reflects subsequent cooling to relatively lower temperatures. The initial cooling ages of syenites, recorded by $^{40}\text{Ar}/^{39}\text{Ar}$ plateau ages clustering at 330 Ma, strikingly resemble those of Saxothuringian K-rich intrusions, reflecting simultaneous ultrapotassic activity in both major tectonic zones of the Bohemian Massif. The short-lived Andean-type subduction of the Saxothuringian domain beneath the continental Moldanubian block is the most likely petrogenetic model of coeval K-rich magmatism in these widely geographically separated tectonic zones.

Acknowledgements

This research was supported by Operational Programme Research, Development and Education [grant number CZ.02.1.01/0.0/0.0/16_026/0008459 (Geobarr) from the European Regional Development Fund] and conducted under institutional support from the Faculty of Science, Masaryk University in Brno. The authors would like to thank Renata Čopjaková and Jakub Haifler (Masaryk University) for technical assistance with EMP analyses and BSE imaging, and Florian Duval (ISTO) with $^{40}\text{Ar}/^{39}\text{Ar}$ data collection. We are indebted to Radek Škoda (Masaryk University) for providing zircon separates. We also gratefully acknowledge constructive comments from two anonymous reviewers and the editorial work of Greg J. G. Shellnutt.

References

- Altherr, R., Meyer, HP., Holl, A., Volker, F., Alibert, C., McCulloch, M.T., Majer, V., 2004. Geochemical and Sr-Nd-Pb isotopic characteristics of late cenozoic leucite lamproites from the east European alpine belt (Macedonia and Yugoslavia). *Contributions to Mineralogy and Petrology* 147, 58–73.
- Avanzinelli, R., Lustrino, M., Mattei, M., Melluso, L., Conticelli, S., 2009. Potassic and ultrapotassic magmatism in the circum-Tyrrhenian region: significance of carbonated pelitic vs. pelitic sediment recycling at destructive plate margins. *Lithos* 113, 213–227.
- Becker, H., Wenzel, T., Volker, F., 1999. Geochemistry of glimmerite veins in peridotites from Lower Austria—implications for the origin of K-rich magmas in collision zones. *Journal of Petrology* 40, 315–338.
- Belousova, E.A., Griffin, W.L., O'Reilly, S.Y., Fisher, M.I. 2002. Apatite as an indicator mineral for mineral exploration: trace-element composition and their relationship to host rock type. *Journal of Geochemical Exploration* 76, 45–60.
- Bohrson, W.A., Spera, F.J., 2001. Energy-Constrained Open-System Magmatic Processes II: Application of energy-constrained assimilation-fractional crystallization (EC-AFC) model to magmatic systems. *Journal of Petrology* 42, 1019–1041.
- Borghini, A., Ferrero, S., O'Brien, P.J., Laurent, O., Günter, C., Ziemann, M.A. 2020. Cryptic metasomatic agent measured in situ in Variscan mantle rocks: melt inclusions in garnet of eclogite, Granulitgebirge, Germany. *Journal of Metamorphic Geology* 38, 207–234.
- Buriánek, D., 2008. Peraluminous granite from the southern edge of the Třebíč Pluton. *Acta Musei Moraviae Scientiae Geologicae* 93, 151–167. (in Czech with English summary).
- Buriánek, D., Ivanov, M., Janderková, J., Patzel, M., 2022. Importance of accessory minerals for the vertical distribution of uranium and thorium in soil profiles: A case study of durbachite from the Třebíč Pluton (Czech Republic). *CATENA* 213, 106166.
- Chu, M.F., Wang, K.L., Griffin, W.L., Chung, S.L., O'Reilly, S.Y., Pearson, N.J., Iizuka, Y., 2009. Apatite composition: tracing petrogenetic processes in Transhimalayan granitoids. *Journal of Petrology* 50, 1829–1855.

- Cochrane, R., Spikings, R.A., Chew, D., Wotzlaw, J.F., Chiaradia, M., Tyrrell, S., Schaltegger, U., Van der Lelij, R., 2014. High temperature (>350 °C) thermochronology and mechanisms of Pb loss in apatite. *Geochimica et Cosmochimica Acta* 127, 39–56.
- Condamine, P., Médard, E., Devidal, J.L., 2016. Experimental melting of phlogopite-peridotite in the garnet stability field. *Contributions to Mineralogy and Petrology* 171, 1–26.
- Condamine, P., Couzinié, S., Fabbrizio, A., Devidal, J.L., Médard, E., 2022. Trace element partitioning during incipient melting of phlogopite-peridotite in the spinel and garnet stability fields. *Geochimica et Cosmochimica Acta* 327, 53–78.
- Conticelli, S., Guarnieri, L., Farinelli, A., Mattei, M., Avanzinelli, R., Bianchini, G., Boari, E., Tommasini, S., Tiepolo, M., Prelević, D., Venturelli, G., 2009. Trace elements and Sr–Nd–Pb isotopes of K-rich, shoshonitic, and calc-alkaline magmatism of the Western Mediterranean Region: genesis of ultrapotassic to calc-alkaline magmatic associations in a post-collisional geodynamic setting. *Lithos* 107, 68–92.
- Conticelli, S., Avanzinelli, R., Ammannati, E., Casalini, M., 2015. The role of carbon from recycled sediments in the origin of ultrapotassic igneous rocks in the Central Mediterranean. *Lithos* 232, 174–196.
- Creaser, R.A., Grutter, H.S., Carlson, J., Crawford, B., 2004. Macrocrystal phlogopite Rb–Sr dates for the Ekati property kimberlites: Evidence for multiple intrusive episodes during Paleocene and Eocene time. *Lithos* 76, 399–414.
- Čopjaková, R., Sulovský, F., Paterson, B.A., 2005. Major and trace elements in pyrope–almandine garnets as sediment provenance indicators of the Lower Carboniferous Culm sediments, Drahany Uplands, Bohemian Massif. *Lithos* 82, 51–70.
- Dallmeyer, R.D., Neubauer, F., Höck, V., 1992. Chronology of late Paleozoic tectonothermal activity in the southeastern Bohemian Massif, Austria (Moldanubian and Moravo-Silesian zones): $^{40}\text{Ar}/^{39}\text{Ar}$ mineral age controls. *Tectonophysics* 210, 135–153.
- Debon, F., Le Fort, P., 1988. A cationic classification of common plutonic rocks and their magmatic associations: principles, method, applications. *Bulletin de Mineralogie* 111, 493–510.

- Donelick, R.A., O'Sullivan, P.B., Ketcham, R.A., 2005. Apatite fission-track analysis. *Reviews in Mineralogy and Geochemistry* 58, 49–94.
- Ersoy, E.Y., Palmer, M.R., 2013. Eocene-Quaternary magmatic activity in the Aegean: Implications for mantle metasomatism and magma genesis in an evolving orogeny. *Lithos* 180, 5–24.
- Foley, S.F., 1992. Vein-plus-wall-rock melting mechanisms in the lithosphere and the origin of potassic alkaline magmas. *Lithos* 28, 435–453.
- Foley, S.F., Prelević, D., Rehfeldt, T., Jacob, D.E., 2013. Minor and trace elements in olivines as probes into early igneous and mantle melting processes. *Earth and Planetary Science Letters* 363, 181–191.
- Förster, M.W., Prelević, D., Schmück, H.R., Buhre, S., Veter, M., Mertz-Kraus, R., Foley, S.F., Jacob, D.E., 2017. Melting and dynamic metasomatism of mixed harzburgite + glimmerite mantle source: implications for the genesis of orogenic potassic magmas. *Chemical Geology* 455, 182–191.
- Förster, M.W., Buhre, S., Xu, B., Prelević, D., Mertz-Kraus, R., Foley, S.F., 2019. Two-stage origin of K-enrichment in ultrapotassic magmatism simulated by melting of experimentally metasomatized mantle. *Minerals* 10, 41. <https://doi.org/10.3390/min10010041>.
- Friedl, G., Finger, F., Paquette, J.L., von Quadt, A., McNaughton, N.J., Fletcher, I.R., 2004. Pre-Variscan geological events in the Austrian part of the Bohemian Massif deduced from U–Pb zircon ages. *International Journal of Earth Sciences* 93, 802–823.
- Gerdes, A., Wörner, G., Finger, F., 2000. Hybrids, magma mixing and enriched mantle melts in post-collisional Variscan granitoids: the Rastenberg Pluton, Austria. In: Franke W, Haak V, Oncken O, Tanner D (Eds.) *Orogenic processes: quantification and modelling in the Variscan Fold Belt*. Geological Society Special Publication 179, pp 415–431.
- Hoskin, P.W., Schaltegger, U., 2003. The composition of zircon and igneous and metamorphic petrogenesis. *Reviews in Mineralogy and Geochemistry* 53, 27–62.
- Janoušek, V., Finger, F., Roberts, M., Frýda, J., Pin, C., Dolejš, D., 2004. Deciphering the petrogenesis of deeply buried granites: whole-rock geochemical constraints on the origin of largely undepleted felsic granulites from the Moldanubian Zone of the Bohemian Massif. In:

- Ishihara S, Stephens WE, Harley SL, Arima M, Nakajima T (Eds.) Fifth Hutton symposium on the origin of granites and related rocks. Geological Society of America Special Papers 389, pp 141–159.
- Janoušek, V., Holub, F.V., 2007. The causal link between HP-HT metamorphism and ultrapotassic magmatism in collisional orogens: case study from the Moldanubian Zone of the Bohemian Massif. *Proceedings of the Geologists' Association* 118, 75–86.
- Janoušek, V., Holub, F.V., Verner, K., Čopjaková, R., Gerdes, A., Hora, J.M., Košler, J., Tyrrell, S. 2019. Two-pyroxene syenitoids from the Moldanubian Zone of the Bohemian Massif: Peculiar magmas derived from a strongly enriched lithospheric mantle source. *Lithos* 342, 239–262.
- Janoušek, V., Hanžl, P., Svojtka, M., Hora, J.M., Kochergina, N.V.I., Gadas, P., Holub, F.V., Gerdes, A., Verner, K., Hrdličková, K., Daly, J.S., Buriánek, D., 2020. Ultrapotassic magmatism in the heyday of the Variscan Orogeny: the story of the Třebíč Pluton, the largest durbachitic body in the Bohemian Massif. *International Journal of Earth Sciences* 109, 1767–1810.
- Jedlička, R., Faryad, S.W., Hauzenberger, C., 2015. Prograde metamorphic history of UHP granulites from the Moldanubian Zone (Bohemian Massif) revealed by major element and Y+REE zoning in garnets. *Journal of Petrology* 55, 2069–2088.
- Jung, S., Hauff, F., Berndt, J., 2020. Generation of a potassic to ultrapotassic alkaline complex in a syn-collisional setting through flat subduction: Constraints on magma sources and processes (Otjimbingwe alkali complex, Damara orogen, Namibia). *Gondwana Research* 82, 267–287.
- Kontonikas-Charos, A., Ehrig, K., Cook, N.J., Ciobanu, C.L., 2019. Crystal chemistry of titanite from the Roxby Downs Granite, South Australia: insights into petrogenesis, subsolidus evolution and hydrothermal alteration. *Contributions to Mineralogy and Petrology* 174, 1–20.
- Košler, J., Konopásek, J., Sláma, J., Vrána, S., 2014. U-Pb zircon provenance of Moldanubian sediments in the Bohemian Massif. *Journal of the Geological Society* 171, 83–95.
- Kotková, J., Schaltegger, U., Leichmann, J., 2010. Two types of ultrapotassic plutonic rocks in the Bohemian Massif—Coeval intrusions at different crustal levels. *Lithos* 115, 163–176.
- Kotková, J., O'Brien, P.J., Ziemann, M.A., 2011. Diamond and coesite discovered in Saxony-type granulite: Solution to the Variscan garnet peridotite enigma. *Geology* 39, 667–670.

- Krmíček, L., Romer, R.L., Ulrych, J., Glodny, J., Prelević, D., 2016 Petrogenesis of orogenic lamproites of the Bohemian Massif: Sr–Nd–Pb–Li isotope constraints for Variscan enrichment of ultra-depleted mantle domains. *Gondwana Research* 35, 198–216.
- Kubeš, M., Leichmann, J., Wertich, V., Mozola, J., Holá, M., Kanický, V., Škoda, R. 2021. Metamictization and fluid-driven alteration triggering massive HFSE and REE mobilization from zircon and titanite: Direct evidence from EMPA imaging and LA-ICP-MS analyses. *Chemical Geology* 586, 120593. <https://doi.org/10.1016/j.chemgeo.2021.120593>.
- Kubeš, M., Leichman, J., Kotková, J., Čopjaková, R., Holá, M., Slíma, J., 2022. Diversity of origin and geodynamic evolution of the mantle beneath the Variscan Orogen indicating rapid exhumation within subduction-related mélangé (Moldanubian Zone, Bohemian Massif). *Lithos* 423, 106726. <https://doi.org/10.1016/j.lithos.2022.106726>.
- Kubínová, Š., Faryad, S.W., Verner, K., Schmitz, M., Holub, F.V., 2017. Ultrapotassic dykes in the Moldanubian Zone and their significance for understanding of the post-collisional mantle dynamics during Variscan orogeny in the Bohemian Massif. *Lithos* 272, 205–221.
- Lardeaux, J.M., Schulmann, K., Faure, M., Janoušek, V., Lexa, O., Skrzypek, E., Edel, J.B., Štípská, P. 2014. The Moldanubian Zone in French Massif Central, Vosges/Schwarzwald and Bohemian Massif revisited: differences and similarities. In: Schulmann, K., Martínez Catalán, J.R., Lardeaux, J.M., Janoušek, V., Oggiano, G. (Eds.) *The Variscan Orogeny: extent, timescale and the formation of the European crust*. Geological Society Special Publication 405, pp 7–44.
- Leichmann, J., Štelcl, J., Zichovalová, K., 1998. The correlation between radioactivity and mineral assemblages: An example from alkali feldspar syenites; Gföhl Unit, Moldanubian Zone. *Acta Musei Moraviae Scientiae Geologicae* 83, 73–84.
- Leichmann, J., 2004. Naloučany: alkali feldspar granite with enigmatic origin. In: Janoušek, V., Holub, F.V., Houzar, S., Jelínek, E., Leichmann, J., Medaris, J.L.G., Novák, M., Vrána, S. (Eds.) *International workshop on petrogenesis of granulites and related rocks. Excursion Guide*. Moravian Museum, Brno, pp 21–23.
- Leichmann, J., Novák, M., Buriánek, D., Burger, D., 2007. High-temperature to ultrahigh-temperature metamorphism related to multiple ultrapotassic intrusions: evidence from garnet–sillimanite–

- cordierite kinzigite and garnet–orthopyroxene migmatites in the eastern part of the Moldanubian Zone. *Geologica Carpathica* 58, 415–425.
- Leichmann, J., Gnojek, I., Novák, M., Sedlák, J., Houzar, S., 2017. Durbachites from the Eastern Moldanubicum (Bohemian Massif): erosional relics of large, flat tabular intrusions of ultrapotassic melts–geophysical and petrological record. *International Journal of Earth Sciences* 106, 59–77.
- Marks, M.A., Markl, G., 2017. A global review on agpaitic rocks. *Earth-Science Reviews* 173, 229–258.
- McDonough, W.F., Sun, S.S., 1995. The composition of the Earth. *Chemical Geology* 120, 223–253.
- McDougall, I., Harrison, T.M., 1999. *Geochronology and thermochronology by the $^{40}\text{Ar}/^{39}\text{Ar}$ method*, 2nd edition. Oxford University Press, Oxford.
- Medaris, J.L.G., Wang, H., Jelínek, E., Mihaljevič, M., Jakes, P., 2005. Characteristics and origins of diverse Variscan peridotites in the Gföhl nappe, Bohemian Massif, Czech Republic. *Lithos* 82, 1–23.
- Middlemost, E.A., 1994. Naming materials in the magma/igneous rock system. *Earth-Science Reviews* 37, 215–224.
- O'Brien, P.J., Rötzler, J., 2003. High-pressure granulites: formation, recovery of peak conditions and implications for tectonics. *Journal of Metamorphic Geology* 21, 3–20.
- Padilla, A.J., Gualda, G.A.R., 2016. Crystal-melt elemental partitioning in silicic magmatic systems: An example from the Peach Spring Tuff high-silica rhyolite, Southwest USA. *Chemical Geology* 440, 326–344.
- Peccerillo, A., Taylor, S.R., 1976. Geochemistry of Eocene calc-alkaline volcanic rocks from the Kastamonu area, northern Turkey. *Contributions to Mineralogy and Petrology* 58, 63–81.
- Perraki, M., Faryad, S.W., 2014. First finding of microdiamond, coesite and other UHP phases in felsic granulites in the Moldanubian Zone: Implications for deep subduction and a revised geodynamic model for Variscan Orogeny in the Bohemian Massif. *Lithos* 202, 157–166.

- Piuzana, D., Castañeda, C., Noce, C.M., Pedrosa Soarez, A.C., Silva, L.C., 2008. Titanite crystal chemistry and U-Pb isotopic data: a petrogenetic indicator for Precambrian granitoid plutons of the eastern Brazilian shield. *Geonomos* 16, 29–36.
- Prelević, D., Foley, S.F., Romer, R.L., Conticelli, S., 2008. Mediterranean Tertiary lamproites derived from multiple source components in post collisional geodynamics. *Geochimica et Cosmochimica Acta* 72, 2125–2156.
- Prelević, D., Akal, C., Foley, S.F., Romer, R.L., Stracke, A., Van Den Bogaard, P., 2012. Ultrapotassic mafic rocks as geochemical proxies for post-collisional dynamics of orogenic lithospheric mantle: the case of southwestern Anatolia, Turkey. *Journal of Petrology* 53, 1019–1055.
- Renne, P.R., Mundil, R., Balco, G., Min, K., Ludwig, K.R., 2010. Joint determination of ^{40}K decay constants and $^{40}\text{Ar}^*/^{40}\text{K}$ for the Fish Canyon sanidine standard, and improved accuracy for $^{40}\text{Ar}/^{39}\text{Ar}$ geochronology. *Geochimica et Cosmochimica Acta* 74, 5349–5367.
- Rudnick, R.L., Fountain, D.M., 1995. Nature and composition of the Continental Crust: a lower crustal perspective. *Reviews of Geophysics* 33, 267–309.
- Schaltegger, U., Gaynor, S.P., Widmann, P., Kotková, J., 2021. Comment on “Ultrapotassic magmatism in the heyday of the Variscan Orogeny: the story of the Třebíč Pluton, the largest durbachitic body in the Bohemian Massif” by Janoušek et al. *International Journal of Earth Sciences*. <https://doi.org/10.1007/s00531-020-01975-w>.
- Schmädicke, E., Gose, J., Vill, T.M., 2010. The P–T evolution of ultra-high temperature garnet-bearing ultramafic rocks from the Saxonian Granulitgebirge Core Complex, Bohemian Massif. *Journal of Metamorphic Geology* 28, 489–508.
- Schulmann, K., Konopásek, J., Janoušek, V., Lexa, O., Lardeaux, J.M., Edel, J.B., Štípská, P., Ulrich, S., 2009. An Andean type Palaeozoic convergence in the Bohemian Massif. *Comptes Rendus Geoscience* 341, 266–286.
- Schulmann, K., Lexa, O., Janoušek, V., Lardeaux, J.M., Edel, J.B., 2014. Anatomy of a diffuse cryptic suture zone: an example from the Bohemian Massif, European Variscides. *Geology* 42, 275–278.

- Sha, L.K., Chappell, B.W., 1999. Apatite chemical composition, determined by electron microprobe and laser-ablation inductively coupled plasma mass spectrometry, as a probe into granite petrogenesis. *Geochimica et Cosmochimica Acta* 63, 3861–3881.
- Shand, S.J., 1943. Eruptive rocks. Their genesis, composition, classification, and their relation to ore-deposits with a chapter on meteorite, 2nd edn. Wiley, New York.
- Shaw, D.M., 1970. Trace element fractionation during anatexis. *Geochimica et Cosmochimica Acta* 34, 237–243.
- Soder, C.G., Romer, R.L., 2018. Post-collisional potassic–ultrapotassic magmatism of the Variscan Orogen: implications for mantle metasomatism during continental subduction. *Journal of Petrology* 59, 1007–1034.
- Stepanov, A., Hermann, J., Rubatto, D., Rapp, R., 2012. Experimental study of monazite/melt partitioning with implications for the REE, Th and U geochemistry of crustal rocks. *Chemical Geology* 300, 200–220.
- Škoda, R., Klementová, M., Čopjaková, R., 2006. Study of zircon from alkali syenite near Naloučany, Moldanubicum, Czech Republic. *Acta Musei Moraviae Scientiae Geologicae* 94, 47–59. (in Czech with English summary).
- Tabaud, A.S., Janoušek, V., Skrzypczak, E., Schulmann, K., Rossi, P., Whitechurch, H., Guerrot, C., Paquette, J.L., 2015. Chronology, petrogenesis and heat sources for successive Carboniferous magmatic events in the southern–central Variscan Vosges Mts. (NE France). *Journal of the Geological Society* 172, 87–102.
- Tajčmanová, L., Konopásek, J., Schulmann, K., 2006. Thermal evolution of the orogenic lower crust during exhumation within a thickened Moldanubian root of the Variscan belt of Central Europe. *Journal of Metamorphic Geology* 24, 119–134.
- von Raumer, J.F., Finger, F., Veselá, P., Stampfli, G.M., 2014. Durbachites–Vaugnerites—a geodynamic marker in the central European Variscan orogen. *Terra Nova* 26, 85–95.
- Were, P., Keppler, H., 2021. Trace element fractionation between biotite, allanite, and granitic melt. *Contributions to Mineralogy and Petrology* 176, 1–14.

- Weber, J., Wilson, B., Koeberl, C., O'Sullivan, P.B., Donelick, R., Posner, E.S., 2019. Reconnaissance reassessment of the late Eocene Oceanic unit, Barbados: Microtektite geochemistry, zircon U-Pb geochronology, micropaleontology, and provenance. *250 Million Years of Earth History in Central Italy: Celebrating 25 Years of the Geological Observatory of Coldigioco* 542, 333–346.
- Wenzel, T., Mertz, D.F., Oberhänsli, R., Becker, T., Renne, P.R., 1997. Age, geodynamic setting, and mantle enrichment processes of a K-rich intrusion from the Meissen massif (northern Bohemian massif) and implications for related occurrences from the mid-European Hercynian. *Geologische Rundschau* 86, 556–570.
- Xu, L., Bi, X., Hu, R., Tang, Y., Wang, X., Xu, Y., 2015. LA-ICP-MS mineral chemistry of titanite and the geological implications for exploration of porphyry Cu deposits in the Jinshajiang–Red River alkaline igneous belt, SW China. *Mineralogy and Petrology* 109, 181–200.
- Zhao, Z., Mo, X., Dilek, Y., Niu, Y., DePaolo, D.J., Robinson, P., Zhu, D., Sun, C., Dong, G., Zhou, S., Luo, Z., Hou, Z., 2009. Geochemical and Sr–Nd–Pb–O isotopic compositions of the post-collisional ultrapotassic magmatism in SW Tibet: petrogenesis and implications for India intra-continental subduction beneath southern Tibet. *Lithos* 113, 190–212.
- Zhong, S., Feng, C., Seltmann, R., Li, D., Gu, H., 2018. Can magmatic zircon be distinguished from hydrothermal zircon by trace element composition? The effect of mineral inclusions on zircon trace element composition. *Lithos* 314, 646–657.
- Žák, J., Verner, K., Jancušek, V., Holub, F.V., Kachlík, V., Finger, F., Hajná, J., Tomek, F., Vondrovič, L., Trubač, J., 2014. A plate-kinematic model for the assembly of the Bohemian Massif constrained by structural relationships around granitoid plutons. *Geological Society Special Publication* 405, 169–196.

Figure captions

Fig. 1 (a) Location of the Bohemian Massif and occurrences of the Variscan basement within the regional frame of western-central Europe (b) Simplified geological map of the eastern Moldanubian Zone hosting widespread ultrapotassic intrusions. Modified on the basis of the Czech Geological Survey on-line maps application (<https://www.geology.cz>)

Fig. 2 Representative hand specimens of major syenite varieties: (a) central (b) marginal (c) nodule. Microphotographs of common mineral assemblages in alkali-rich syenites: (d) significant amount of metamict zircon typically surrounded by abundant microfractures (central variety; plane-polarized light) (e) subhedral amphibole enclosed in perthitic K-feldspar (marginal variety; plane-polarized light). Abbreviations: Kfs = K-feldspar, Zrn = zircon, Amp = amphibole

Fig. 3 (a) Characteristic zircon morphology from all alkali-rich syenites (central variety; SEM image) (b) Strongly metamict zircon showing dissolution-reprecipitation textures particularly within its crystal interiors, containing early magmatic U-thorite inclusions (central variety; BSE image) (c) Partially altered zircon typically displaying low BSE intensity (nodule variety; BSE image) (d) Inclusion-free zircon exhibiting only limited effects of alteration (marginal variety; BSE image) (e) Subhedral titanite with sector zoning within the core and oscillatory zonation in rims (marginal variety; BSE image) (f) Euhedral apatite showing weak oscillatory zoning in the crystal core (marginal variety; BSE image). Abbreviations: Zrn = zircon, U-Thr = U-thorite, Bt = biotite, Kfs = K-feldspar, Chl = chlorite, Ttn = titanite, Amp = amphibole, Ap = apatite

Fig. 4 (a) Binary plot $^{0}(\text{Al} + 2\text{Ti})$ vs. $^{\text{A}}(\text{Na} + \text{K})$ and (b) $\text{Mg}\#$ [$\text{Mg}/(\text{Mg} + \text{Fe})$] vs. ^{IV}Al diagram showing compositional variations in amphiboles from individual syenite varieties compared to amphibole chemistry from the ultrapotassic Třebíč pluton (Janoušek et al., 2020). Amphiboles from direct contact between central and marginal variety are marked in the $\text{Mg}\#$ vs. ^{IV}Al plot (see Section 5.1. for details)

Fig. 5 (a–c) Chondrite-normalized (McDonough and Sun, 1995) REE patterns of accessory phases

Fig. 6 Classification diagrams for syenite varieties (a) Binary plot SiO_2 vs. $\text{Na}_2\text{O} + \text{K}_2\text{O}$ (Middlemost, 1994) (b) SiO_2 vs. K_2O (Peccerillo and Taylor, 1976) (c) A/CNK vs. A/NK (Shand, 1943) (d) Multicationic plot B vs. Mg# (Debon and Le Fort, 1988). The whole-rock composition of ultrapotassic rocks of the Třebíč pluton (TP) and its marginal facies (Janoušek et al., 2020) along with lamproites (Krmíček et al., 2016) from the Bohemian Massif is illustrated for comparison

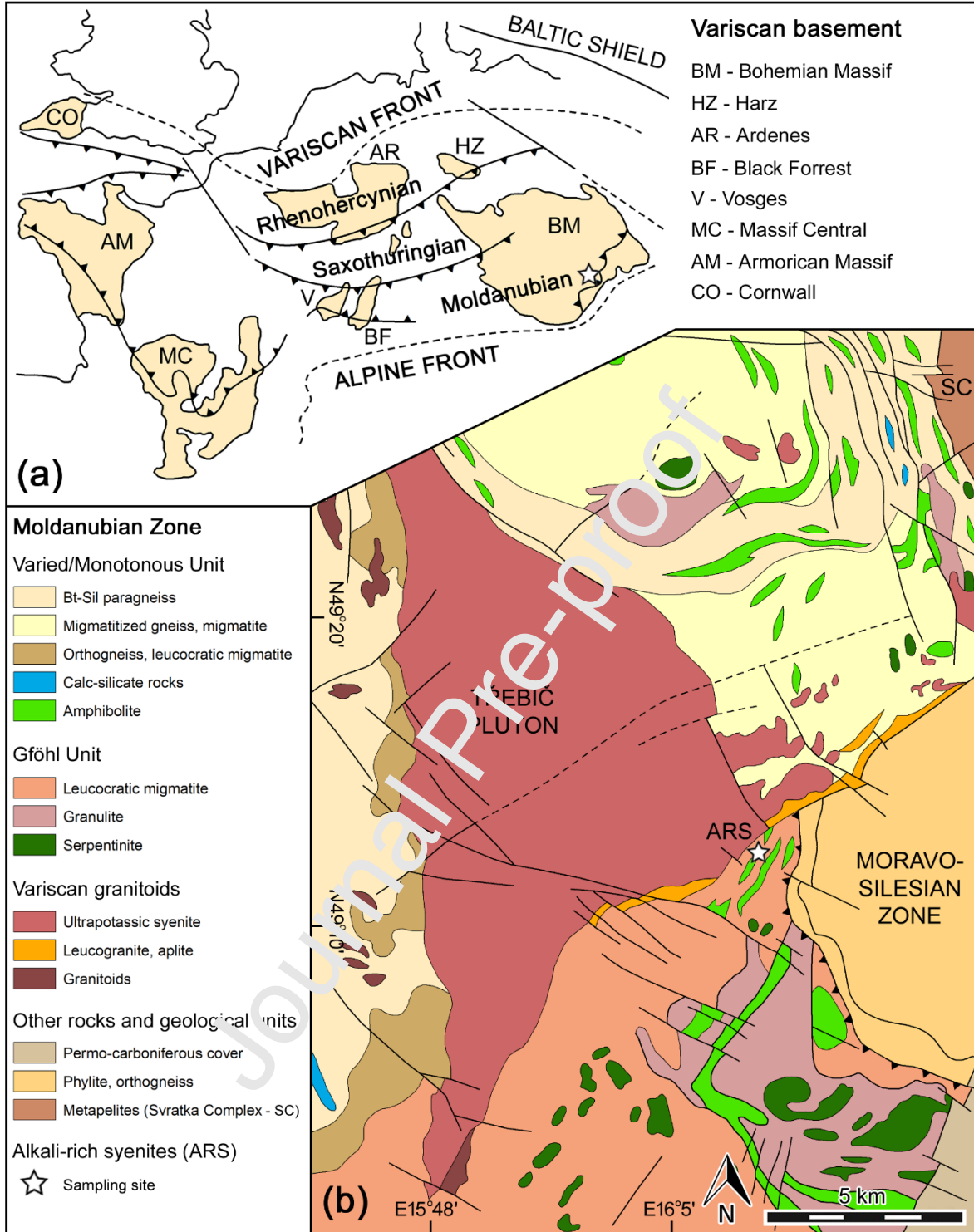
Fig. 7 (a) Chondrite-normalized REE patterns and (b) primitive-mantle-normalized multielement spider plot for syenite varieties, standardized values are from McDonough and Sun (1995). Grey compositional fields for ultrapotassic rocks of the Třebíč pluton based on data from Janoušek et al. (2020). (c) Results of trace element-based partial melting models. Grey-blue and hatched fields show the composition glimmerite and melt generated by glimmerite melting experiments at 10 kbar and 1125 °C respectively (Förster et al., 2017). Red lines show melt compositions modelled by 0.1 and 5 % (red numbers denote the amount of melt in %) batch melting of a phlogopite-bearing mantle source (composition as that proposed by Förster et al. 2017). Source was 0.45 olivine, 0.30 clinopyroxene, 0.20 phlogopite, and 0.15 orthopyroxene; with melting proportions of 0.30 olivine, 0.20 clinopyroxene, 0.40 phlogopite, and 0.10 orthopyroxene. Mineral/melt distribution coefficients used in the modelling are from Condamine et al. (2022). Green line showing results of the best-fit AFC model. This model requires a total of 5 % (green number denotes the amount of melt in %) fractional crystallization in combination with assimilation (assimilation rate/fractionation rate is 0.8) of leucogranitic melts generated by partial melting of the Moldanubian crust (sample III; Buriánek 2008). The fractionating mineral assemblage from melt generated by 1 % batch melting of a phlogopite-bearing mantle source was modeled as Pl (60 %) + Bt (35 %) + Mnz (1 %) + Ap (0.5 %) + Aln (0.5 %), and mineral/melt distribution coefficients are taken from Stepanov et al. (2012), Padilla et al. (2016), Were et al. (2021)

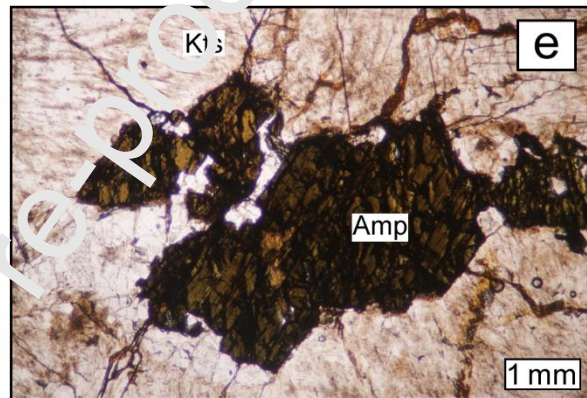
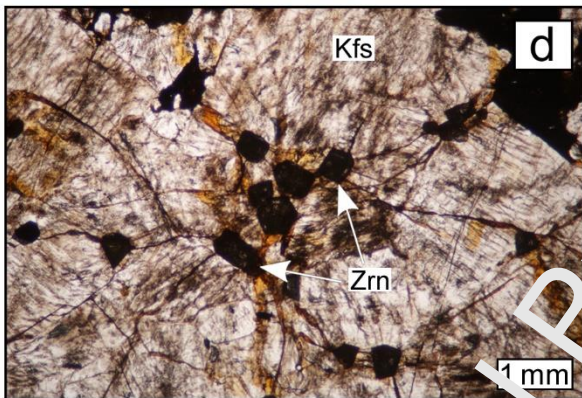
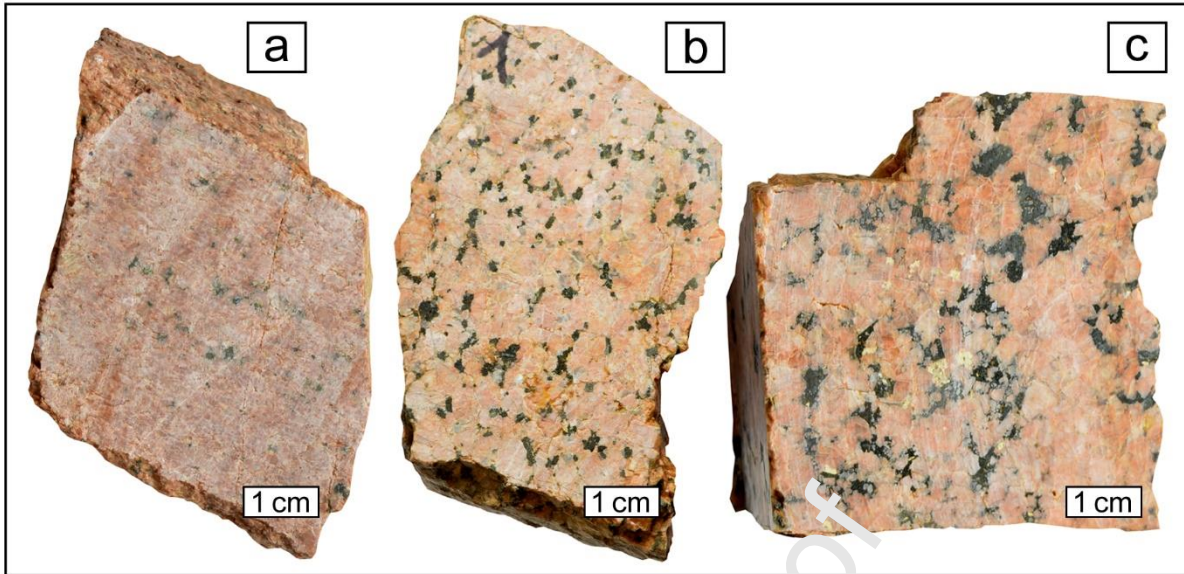
Fig. 8 (a) Binary plot $^{87}\text{Sr}/^{86}\text{Sr}_{335}$ vs. ϵNd_{335} illustrating the isotopic composition of the miaskitic syenites relative to other mantle and crustal lithologies from the Moldanubian Zone together with hybrid rocks of glimmerite veins and the durbachitic Třebíč pluton (TP), adapted after Janoušek et al. (2020). (b) Zoomed part binary plot of $^{87}\text{Sr}/^{86}\text{Sr}_{335}$ vs. ϵNd_{335} showing the possible mixing hyperbola

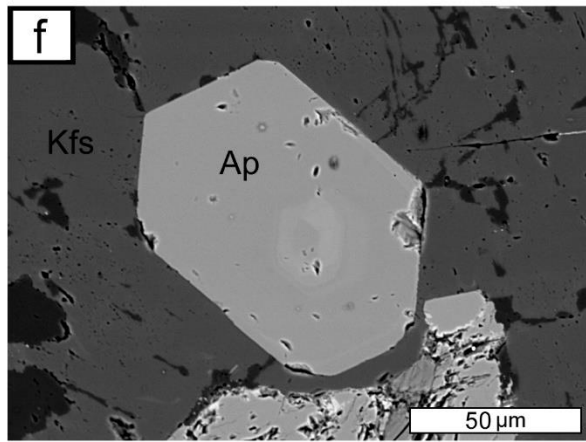
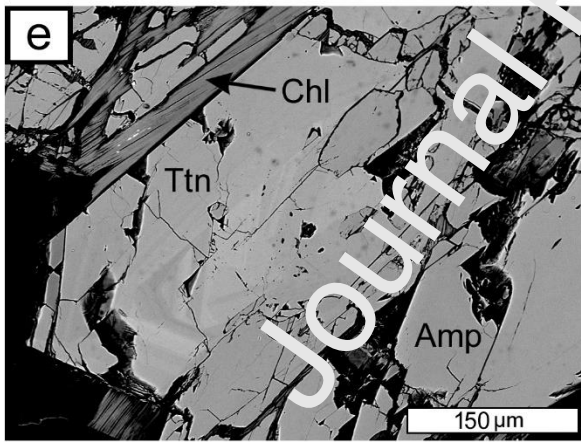
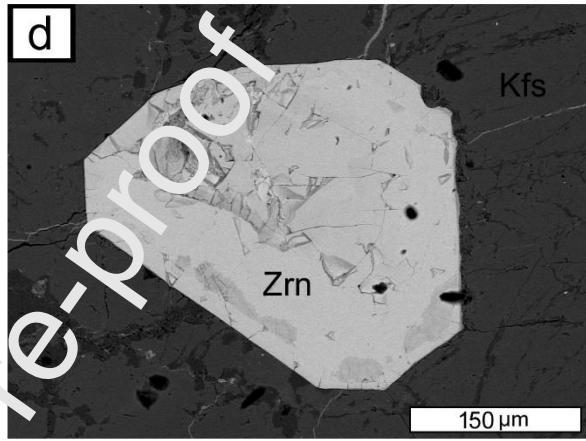
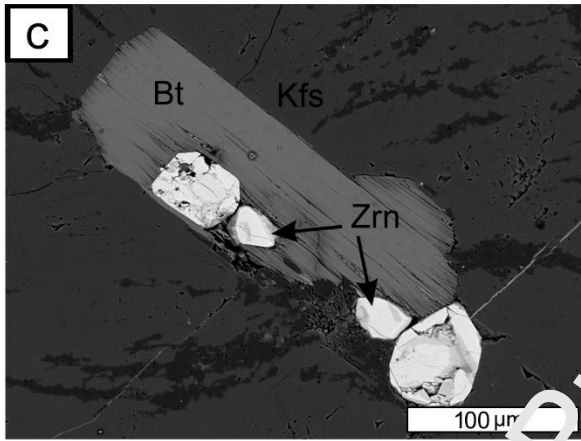
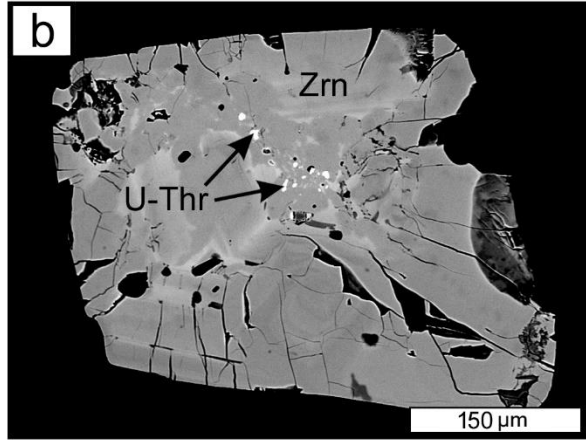
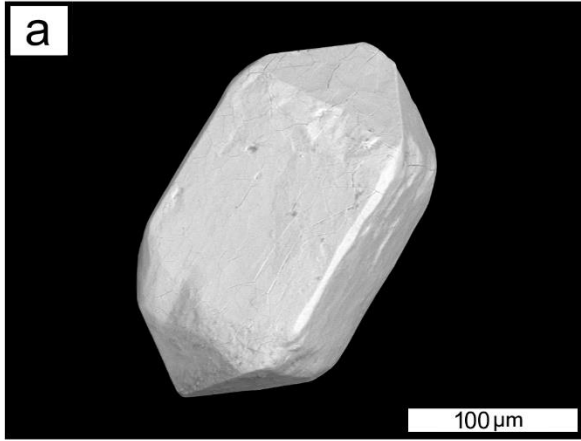
between the crustal contaminant and enriched mantle source for durbachitic analyses from the Třebíč Pluton according to Janoušek et al. (2020). (c) Binary Ba vs. Rb and (d) Ce vs. Rb/Sr (logarithmic scale) diagrams show result batch melting modelling of a phlogopite-bearing mantle source (red vector correspond to 30 % melting mantle source) and assimilation and fractional crystallization (AFC) modelling (green vector correspond to 5 % fractionation). Details of modelling are the same as reported in Fig. 7c, and the number denotes the amount of melt in %. Grey-blue and hatched fields show the composition glimmerite and melt generated by glimmerite melting experiments at 10 kbar and 1125 °C respectively (Förster et al. 2017). PM = primitive-mantle composition values are from McDonough and Sun (1995)

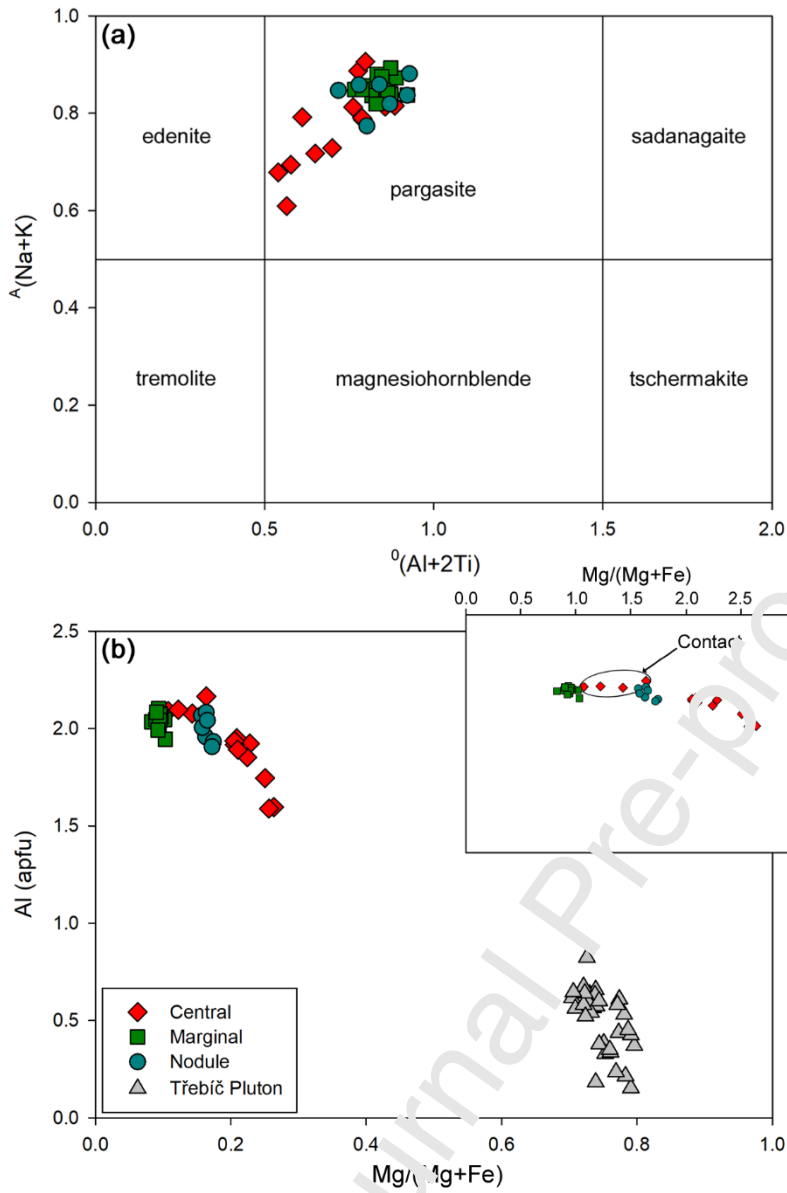
Fig. 9 Tera-Wasserburg concordia diagram with results of apatite dating; grey band represents the U decay constant uncertainty. MSWD = mean square of weighted deviations

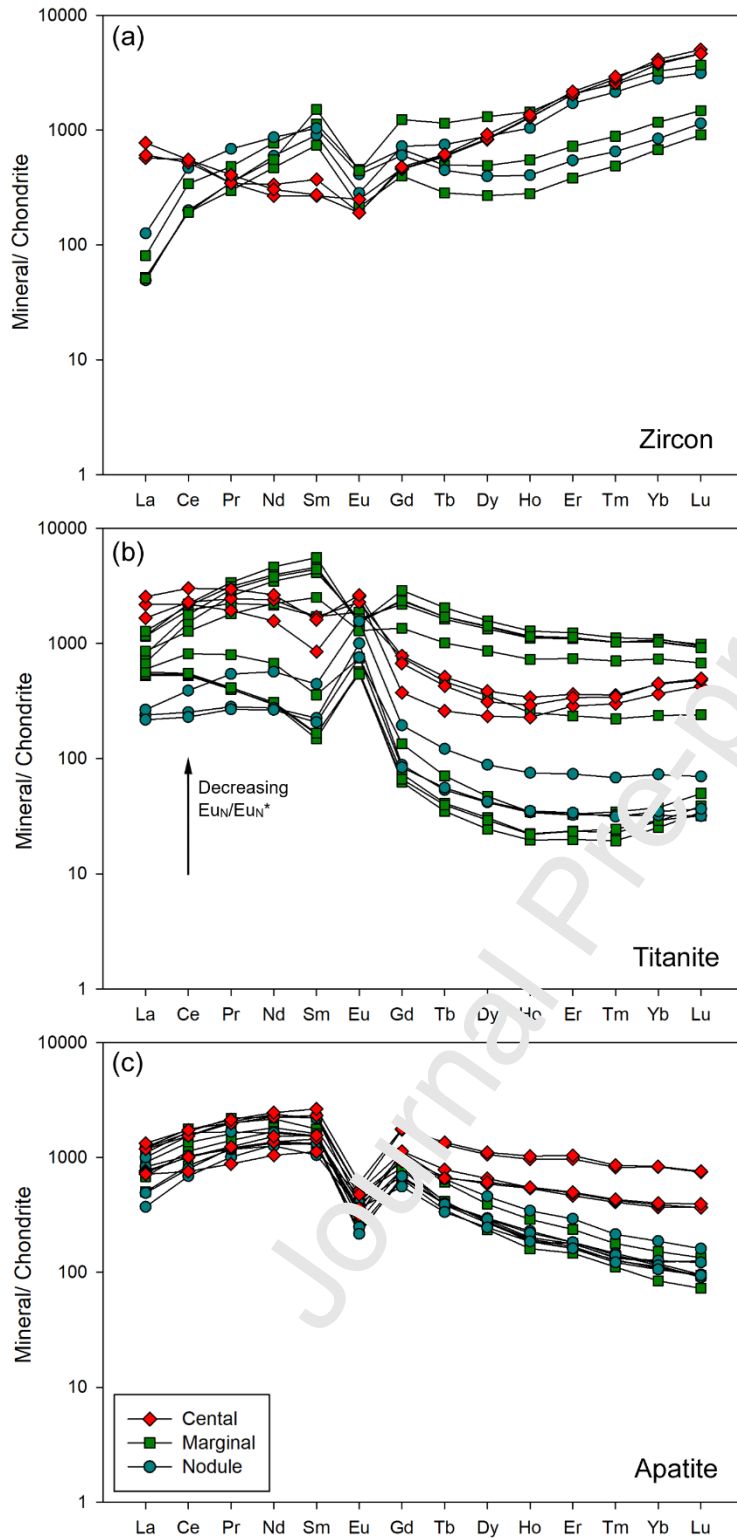
Fig. 10 Results of $^{40}\text{Ar}/^{39}\text{Ar}$ dating for (a) amphibole and (b) biotite from miaskitic syenites. PA = plateau ages, MSWD = mean square of weighted deviations

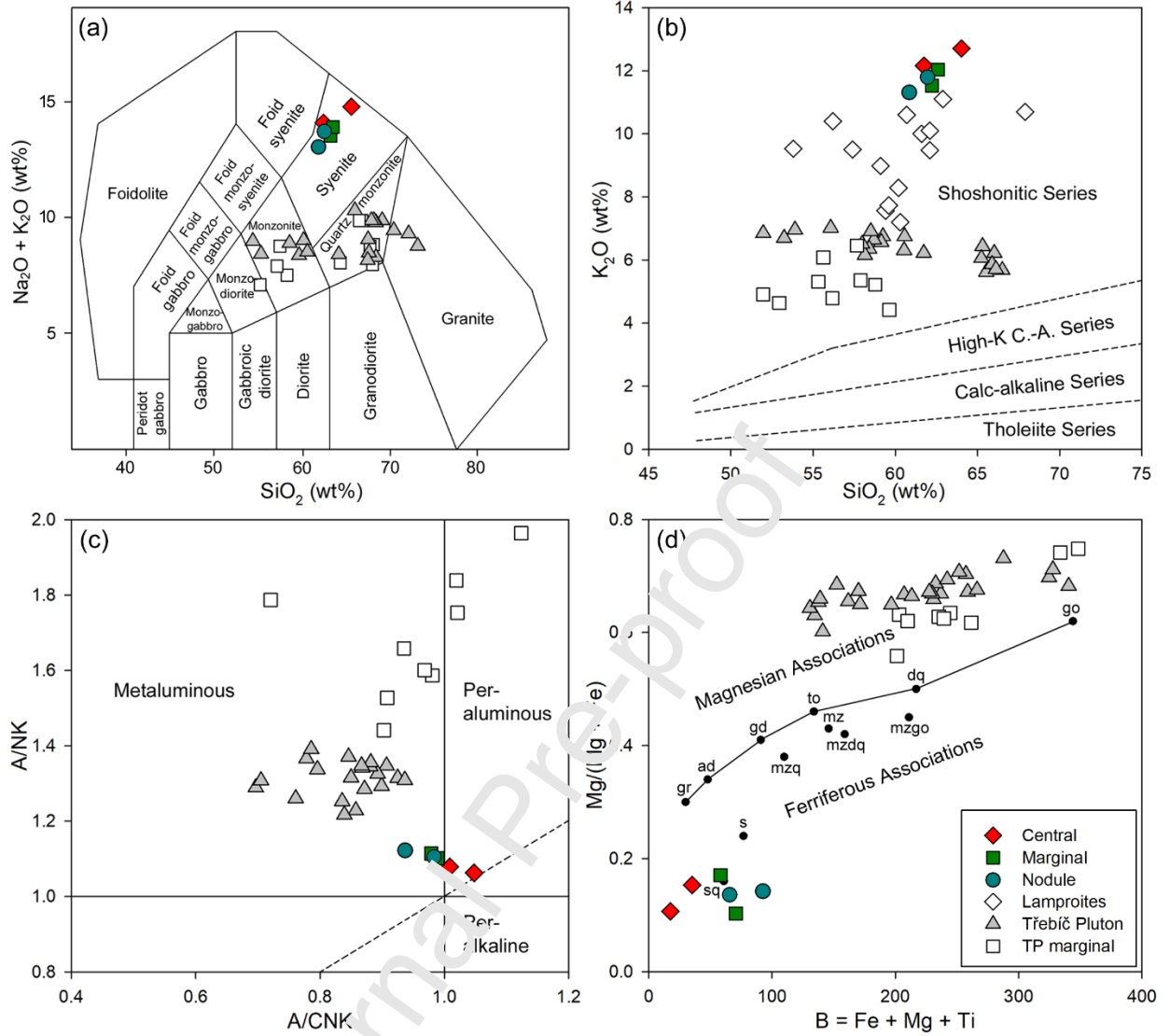


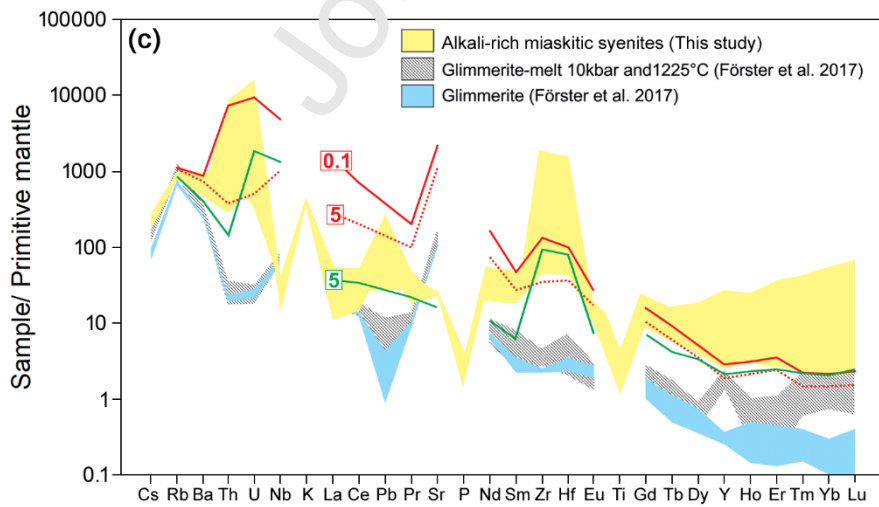
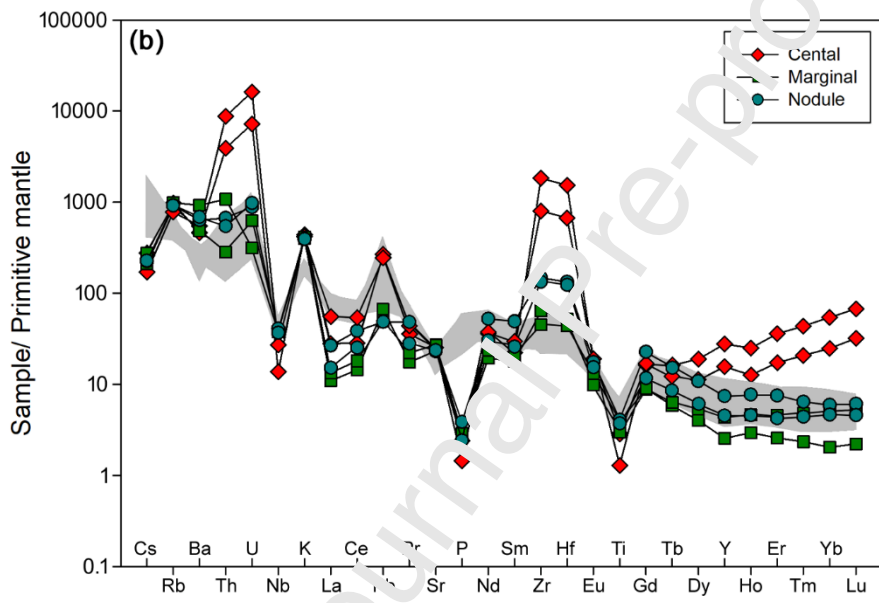
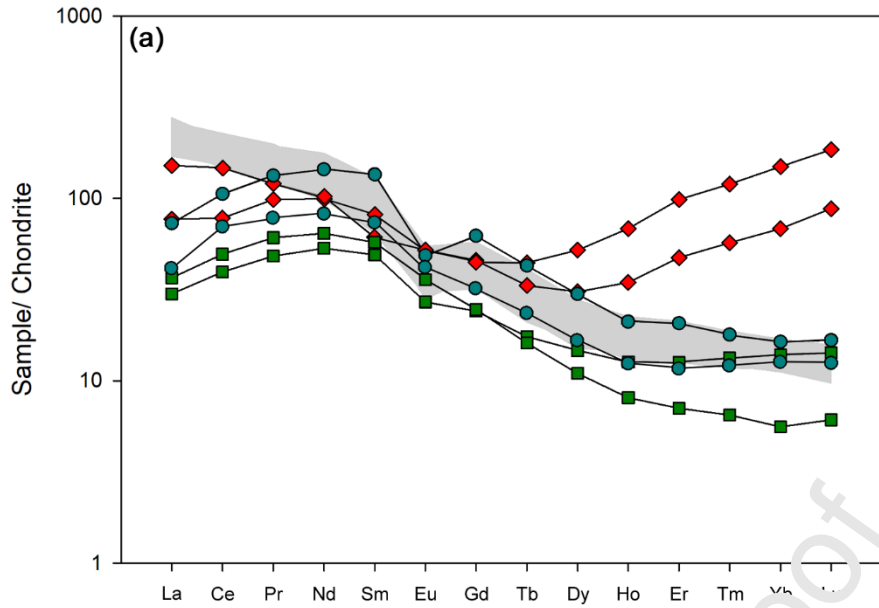


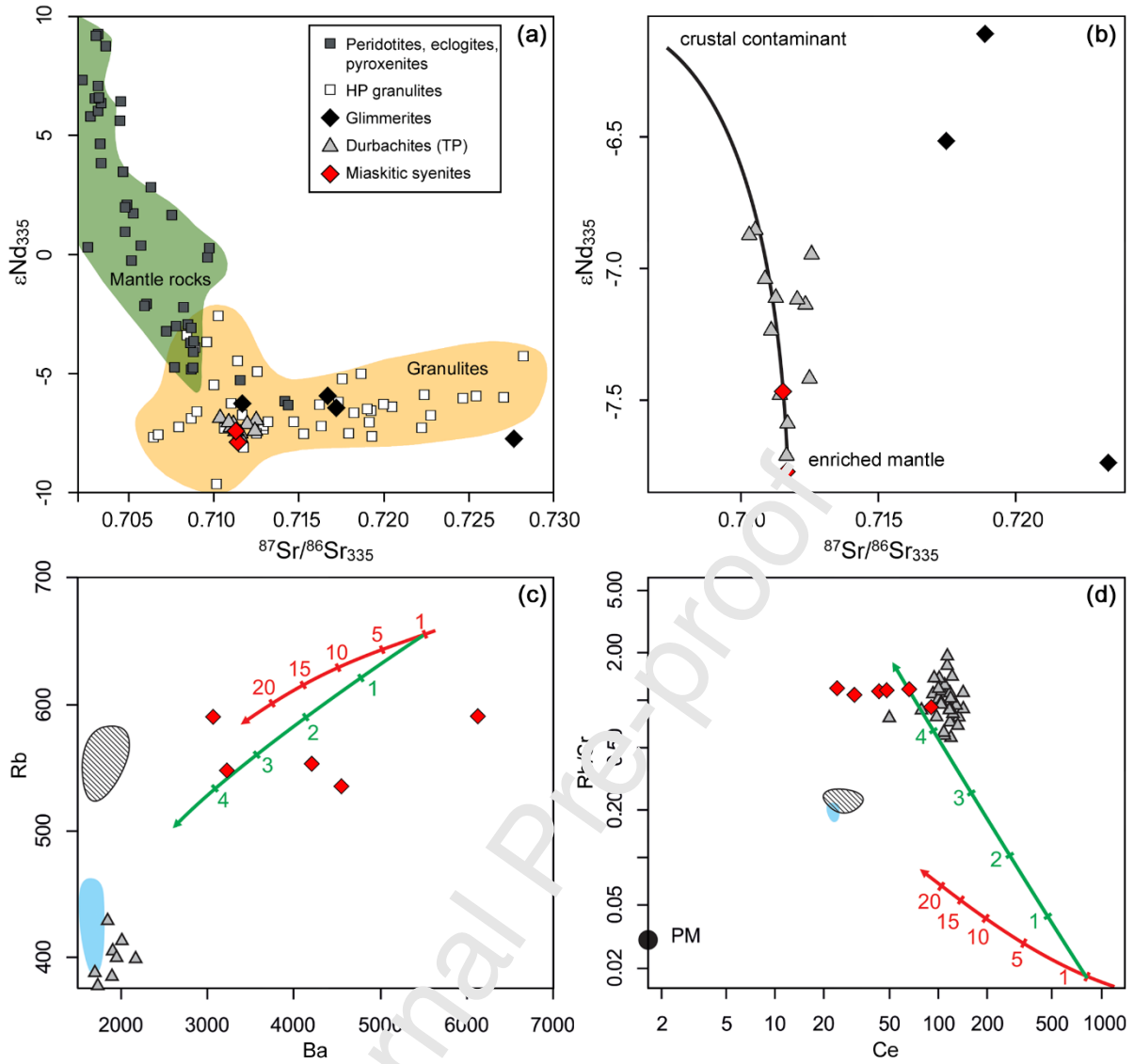


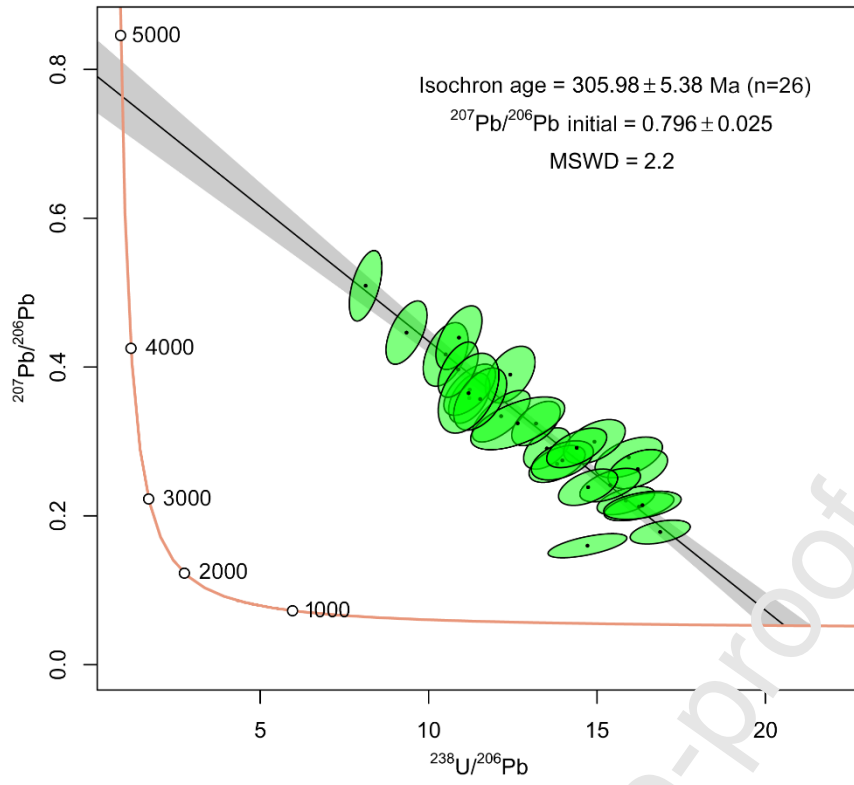












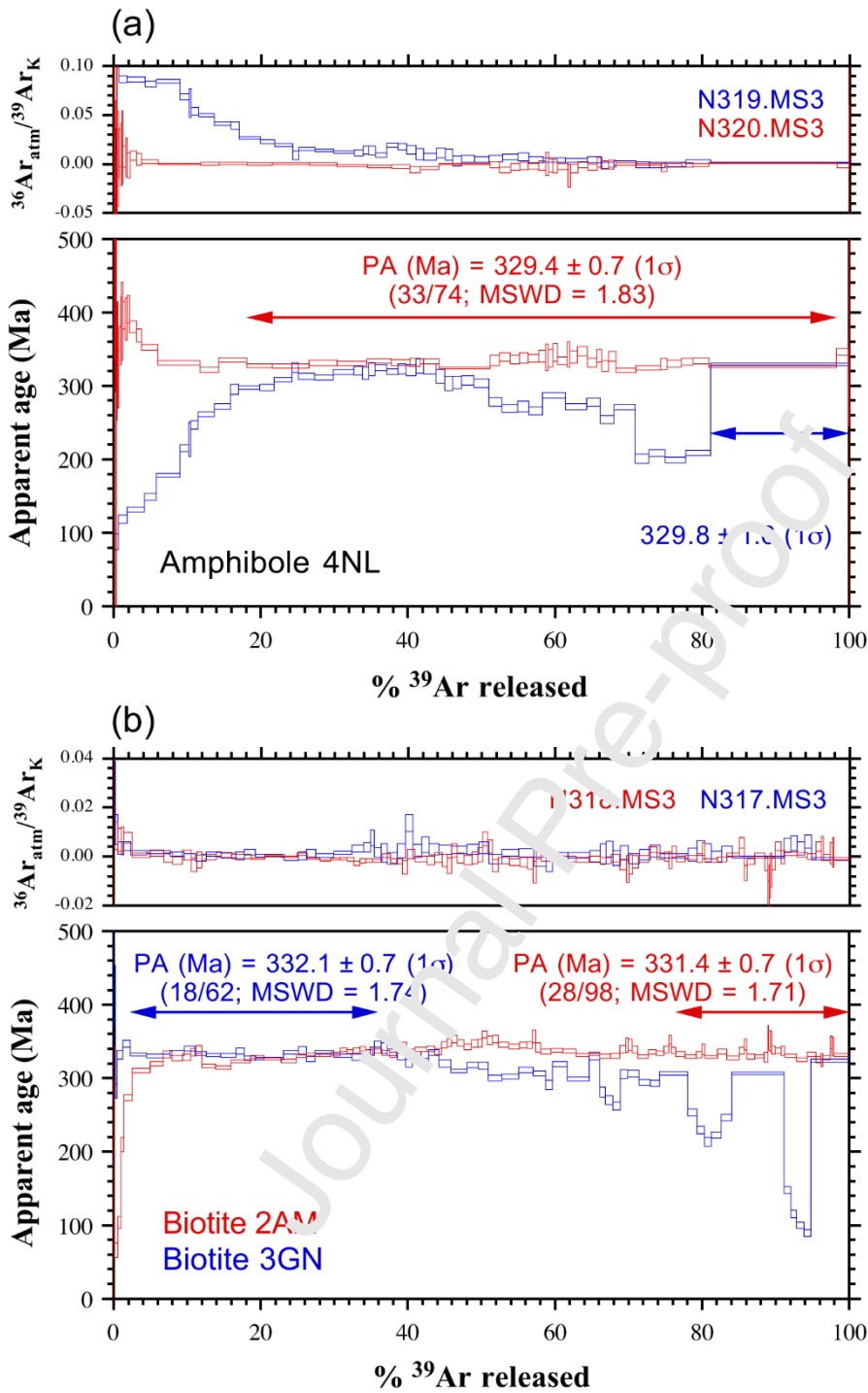


Table 1 EMP analy

Mineral	K-feldspar		Plagioclase				Amphibole				Biotite				Chlorite													
	Central	Central	Marginal	Marginal	Nodule	Nodule	Marginal	Marginal	Nodule	Nodule	Central	Central	Marginal	Marginal	Nodule	Nodule	Central	Marginal	Nodule									
Variety	1	1	1	1	e	e	1	1	e	e	1	1	1	1	e	e	1	1	1	1	e	e	1	1	e			
Major oxides (wt%)																												
SiO ₂	64.58	65.23	64.45	64.95	65.25	64.94	68.16	67.82	68.65	68.02	42.94	41.03	38.82	38.34	38.61	39.81	39.19	38.40	33.89	35.09	33.56	34.89	34.34	33.43	25.29	29.03	25.71	
TiO ₂											1.06	1.94	2.10	2.37	2.26	2.49	2.51	1.88	2.72	3.53	6.00	5.99	6.09	5.94	0.26	0.07	0.13	
Al ₂ O ₃	18.30	18.48	18.31	18.47	18.23	18.75	20.14	20.78	20.09	19.63	8.66	10.40	11.06	10.91	10.55	11.05	11.26	11.42	14.55	14.42	13.43	14.07	13.71	14.35	18.86	16.49	17.38	
FeO	b.d.l.	b.d.l.	b.d.l.	0.07	b.d.l.	b.d.l.	b.d.l.	b.d.l.	b.d.l.	0.12	25.91	26.95	29.39	29.87	28.12	28.39	29.60	27.62	33.22	29.90	32.84	30.52	29.99	30.47	40.26	33.81	40.57	
MgO											5.20	3.91	1.70	1.77	2.96	3.16	2.32	3.03	3.73	3.22	1.73	2.27	3.79	2.37	5.79	5.91	4.81	
CaO	b.d.l.	b.d.l.	b.d.l.	b.d.l.	b.d.l.	0.06	0.92	1.30	0.77	0.44	11.58	11.54	11.18	11.29	11.60	11.32	11.43	11.43	b.d.l.	0.10	b.d.l.	0.08	b.d.l.	0.09	b.d.l.	0.40	0.17	
MnO											0.49	0.53	0.49	0.50	0.41	0.49	0.50	0.55	0.24	0.28	0.31	0.19	0.30	0.27	0.38	0.38	0.46	
BaO	0.55	0.49	0.42	0.41	0.57	0.64	b.d.l.	b.d.l.	b.d.l.	b.d.l.	b.d.l.	b.d.l.	b.d.l.	b.d.l.	b.d.l.	b.d.l.	0.17	b.d.l.	b.d.l.	0.11	0.43	0.40	0.52	0.40				
K ₂ O	16.19	15.31	16.23	15.27	15.16	14.23	0.14	0.15	0.13	0.11	1.12	1.61	1.99	2.17	1.92	1.87	1.99	2.11	7.46	8.88	9.07	8.80	8.90	8.09	0.39	0.69	0.16	
Na ₂ O	0.39	1.33	0.38	1.25	1.24	1.44	11.11	11.06	10.96	11.17	1.27	1.53	1.55	1.28	1.48	1.46	1.36	1.32	b.d.l.	b.d.l.	b.d.l.	0.08	0.10	0.12	b.d.l.	0.11	b.d.l.	
F	b.d.l.	b.d.l.	b.d.l.	b.d.l.	b.d.l.	b.d.l.	b.d.l.	b.d.l.	0.09	b.d.l.	0.17	0.10	0.10	b.d.l.	0.10	0.09	b.d.l.	0.11	0.11	b.d.l.	b.d.l.	b.d.l.	b.d.l.	b.d.l.				
Cl											0.29	0.27	0.38	0.39	0.35	0.34	0.4	0.37	0.41	0.55	0.29	0.30	0.31	0.25				
Total	100.0	100.8	99.8	100.4	100.4	100.1	100.5	101.1	100.7	99.5	98.7	101.6	98.7	100.6	98.4	102.4	102.2	100.2	96.3	96.1	97.7	101.3	98.1	99.6	91.2	86.9	89.4	
Cation proportions (apfu)																												
Si	2.996	2.984	2.994	2.984	3.001	2.998	2.974	2.940	2.989	2.996	6.720	6.417	6.260	6.196	6.226	6.41	6.192	6.178	2.743	2.821	2.711	2.768	2.717	2.701	2.784	3.320	2.916	
Ti											0.124	0.229	0.255	0.288	0.274	0.254	0.298	0.227	0.166	0.213	0.365	0.358	0.362	0.361	0.021	0.006	0.011	
Al	1.001	0.996	1.002	1.000	0.988	1.020	1.035	1.062	1.031	1.019	1.597	1.917	2.103	2.078	2.06	2.042	2.097	2.165	1.388	1.366	1.279	1.316	1.278	1.366	2.447	2.223	2.324	
Fe	0	0	0	0.003	0	0	0	0	0	0.004	3.391	3.525	3.964	4.038	3.792	3.722	3.910	3.716	2.248	2.010	2.219	2.025	1.984	2.059	3.707	3.234	3.848	
Mg											1.213	0.912	0.407	0.427	0.711	0.738	0.545	0.727	0.450	0.386	0.208	0.268	0.447	0.285	0.951	1.007	0.813	
Ca	0	0	0	0	0	0.003	0.043	0.060	0.036	0.021	1.942	1.933	1.931	1.955	2.005	1.902	1.935	1.970	0	0.009	0	0.007	0	0.008	0	0.048	0.021	
Mn											0.065	0.071	0.078	0.069	0.056	0.065	0.067	0.075	0.017	0.019	0.021	0.013	0.020	0.019	0.035	0.037	0.044	
Ba	0.010	0.009	0.008	0.007	0.010	0.012	0	0	0	0	0	0	0	0	0	0	0.011	0	0	0.004	0.013	0.012	0.016	0.013				
K	0.958	0.893	0.962	0.895	0.889	0.838	0.008	0.008	0.007	0.006	0.223	0.322	0.309	0.447	0.395	0.375	0.400	0.432	0.770	0.911	0.935	0.890	0.898	0.834	0.055	0.101	0.023	
Na	0.035	0.118	0.035	0.111	0.111	0.129	0.940	0.930	0.925	0.954	0.386	0.467	0.486	0.402	0.463	0.444	0.415	0.474	0	0	0	0.012	0.016	0.018	0	0.024	0	
F	0	0	0	0	0	0	0	0	0.012	0	0.02	0.056	0.050	0	0.053	0.046	0	0.055	0.029	0	0	0	0	0				
Cl											0.078	0.071	0.103	0.106	0.097	0.091	0.111	0.128	0.057	0.075	0.040	0.040	0.041	0.034				
Fe/(Fe+Mg)											0.74	0.79	0.91	0.90	0.84	0.83	0.88	0.84	0.83	0.84	0.91	0.88	0.82	0.88	0.80	0.76	0.83	
Mg#											0.26	0.21	0.09	0.10	0.16	0.17	0.12	0.16	0.17	0.16	0.09	0.12	0.18	0.12	0.20	0.24	0.17	
An %	0	0	0	0	0	0.3	4.4	6.0	3.5	2.1																		
Ab %	3.5	11.7	3.5	11.0	11.1	13.3	94.9	93.1	95.2	97.3																		
Or %	96.5	88.3	96.5	89.0	88.9	86.4	0.8	0.8	0.7	0.6																		

Cation proportions calculated based on a total of five (feldspars), ten (chlorite) cations and eleven (biotite), twenty-four (amphibole) oxygen atoms per formula unit

FeO in amphibole, biotite, and chlorite corresponds to total iron oxide content

*Direct contact between central and marginal variety (see text for details)

b.d.l.: below detection limits

Empty entries: not determined

Table 2

Mineral Variety	Apatite			Ilmenite								
	Central	Central	Central	Marginal	Marginal	Marginal	Nodule	Nodule	Nodule	Central	Marginal	Nodule
Major oxides (wt%)												
SiO ₂	0.44	0.44	0.67	0.27	0.62	0.18	0.25	0.28	0.29	b.d.l.	b.d.l.	b.d.l.
TiO ₂										51.79	52.12	51.01
Ce ₂ O ₃	0.17	b.d.l.	0.17	0.16	0.29	b.d.l.	0.19	b.d.l.	b.d.l.			
Dy ₂ O ₃												
Y ₂ O ₃	b.d.l.	0.35	0.44	b.d.l.	0.15	b.d.l.	b.d.l.	b.d.l.	0.23			
P ₂ O ₅	42.41	42.48	41.52	41.23	41.74	42.60	41.94	43.03	42.43			
Nb ₂ O ₅										0.20	0.13	0.21
FeO	0.08	b.d.l.	0.09	0.11	0.12	0.21	0.08	b.d.l.	0.21	46.61	46.23	46.00
CaO	55.85	55.38	54.94	55.04	54.54	55.44	55.57	55.27	55.56	0.04	0.07	b.d.l.
MnO	0.12	0.09	0.08	0.10	0.08	0.07	0.11	0.08	0.07	1.96	2.11	2.77
F	3.64	3.59	3.56	3.76	3.59	3.85	3.55	3.74	3.16			
Cl	0.16	0.10	0.17	0.28	0.14	0.13	0.20	0.14	0.14			
Total	102.9	102.4	101.6	101.0	101.3	102.5	101.9	102.6	102.1	100.6	100.7	100.0
Cation proportions (apfu)												
Si	0.036	0.037	0.057	0.02	0.052	0.015	0.021	0.024	0.024	0	0	0
Ti										0.977	0.983	0.978
Ce	0.005	0	0.005	0.005	0.009	0	0.006	0	0			
Dy												
Y	0	0.016	0.020	0	0.007	0	0	0	0.010			
P	2.974	2.987	2.953	2.967	2.971	3.002	2.977	3.017	2.987			
Nb										0.002	0.002	0.002
Fe	0.005	0	0.006	0.008	0.008	0.015	0.005	0	0.015	0.978	0.969	0.970
Ca	4.958	4.929	4.946	5.013	4.914	4.945	4.993	4.905	4.950	0.001	0.002	0
Mn	0.008	0.006	0.006	0.007	0.006	0.005	0.008	0.006	0.005	0.042	0.045	0.059
F	0.954	0.942	0.947	1.010	0.954	1.013	0.941	0.960	0.830			
Cl	0.022	0.014	0.025	0.040	0.021	0.019	0.029	0.019	0.020			

Cation proportions calculated based on a total of three (ilmenite), four (zircon, U-thorite), five (titanite), and twelve (apatite) oxygen atoms per formula unit

b.d.l.: below detection limits

Empty entries: not determined

Table 3 LA-ICP-MS

Mineral Variety	Granite									Apatite																				
	Zircon Central	Zircon Central	Zircon Central	Marginal	Marginal	Marginal	Nodule	Nodule	Nodule	Central	Central	Marginal	Marginal	Marginal	Nodule	Nodule	Nodule	Central	Central	Central	Marginal	Marginal	Marginal	Nodule	Nodule	Nodule				
Sc	528	470	527	583	511	504	464	440	388	7.6	12.2	17.6	10	15.2	25.2	21.6	27.7	34.9	b.d.l.	b.d.l.	b.d.l.	5.9	2	b.d.l.	1.5	b.d.l.	1.1			
Ga	4.4	4	4.1	2.8	1.7	2.1	3.7	1.0	0.8	15.5	14.9	15.3	18	13.7	18.8	6.9	5.7	6.7	9.6	11.6	4.4	7	10.6	11.5	5.9	5.6	9.8			
Ge	5.9	5.1	5.1	4.1	3.0	2.7	5.8	b.d.l.	b.d.l.	20.4	16.0	16.4	26	17.3	21.9	9.2	6.8	6.9	11	13.2	4.6	7.5	12.2	15.5	6.6	4.7	12			
Sr	18.6	12.5	80.8	3.1	1.1	1.5	1.3	1.1	0.5	28.5	26.9	29.9	20.6	20.6	23	25.9	27.6	26.0	211	196	138	311	274	266	286	218	245			
Y	2090	2357	2161	2291	446	578	697	1277	192.0	475	812	353	1597	996	1434	99.8	37	45.5	1472	1560	630	238	281	397	331	161	496			
Zr	41858	46567	41910	455701	479897	488165	49093	45940	46051	9	2	8	136	417	405	221	299	456	131	131	1040	1.3	1.5	0.2	12.8	0.5	1.5	3.4	13.5	6.5
Nb	57.4	49.8	52.7	8.25	4.6	5.4	4.5	5.4	1.6	1026	680	1049	1124	587	712	763	679	453	b.d.l.	b.d.l.	b.d.l.	0.6	b.d.l.	0.1	b.d.l.	b.d.l.	b.d.l.			
La	135	184	143	12.1	10.3	11.6	29.9	15.0	3.5	392	240	273	191	162	234	62.8	124	51.4	279	315	164	119	214	260	116	191	237			
Ce	339	338	320	118	107	121	287	96.3	36.3	1398	1032	1190	1086	738	1054	238	321	140	941	1061	432	519	825	1030	487	615	947			
Pr	31.9	37.9	31.9	32.5	21.8	26.4	63.5	15.0	10.1	226	192	206	272	163	238	50.2	37	24.8	183	198	67.5	109	149	203	112	98.9	190			
Nd	153	139	122	252	169	200	395	91.6	83.7	1093	970	981	1733	1007	1464	259	136	721	729	1121	391	610	827	1030	623	501	1081			
Sm	55	40	39.6	224	84.0	96.4	153	49.1	45.3	251	257	253	649	365	548	65.7	24.1	10.6	342	390	138	192	238	328	196	110	325			
Eu	10.8	11	14.0	24.9	11.5	11.6	23.1	10.5	5.8	128	79.1	105	86.1	71.4	76.3	87.4	3.8	42.6	28.9	33.8	26.2	12.8	18.6	22.3	14	15	28.7			
Gd	90.9	95.2	91.7	245	65.9	73.2	119	70.2	31.1	155	176	150	465	237	378	38.6	14.7	16.7	345	352	141	128	156	209	132	74	221			
Tb	21.2	22.2	21.6	41.5	9.0	10.2	16.1	14.5	3.6	18.5	23.4	16.8	61.4	32.4	50.2	15.7	1.5	2.0	46.5	48.7	17.1	12.6	13.9	21.9	14.2	7.4	23.3			
Dy	203	226	207	321	59.3	72	97.2	129	25	94.9	142	86.6	347	190	284	21.7	7.5	10.4	260	272	109	57.9	66	96.3	72.7	38.3	113			
Ho	69.9	74.2	70.8	78.63	15.4	18.7	22	38.6	6.5	18.6	30.2	13.6	62.9	37.3	52.9	4.10	1.2	1.9	52.6	56.1	23.4	8.8	10.4	15.8	12.5	5.9	18.7			
Er	327	346	325	332	60.4	72.3	86.9	169	27.2	57.8	99.8	37.7	180	107	15	11.7	3.8	5.4	155	166	64	23.5	25.7	37.7	29.2	14.3	46.7			
Tm	63.1	72.0	68.8	62.1	12	14.4	16.1	34.8	6	8.79	14.8	5.5	25.3	15.1	22.4	1.69	0.6	0.8	20.2	21.1	8.1	2.75	3.2	4.4	3.6	1.7	5.3			
Yb	604	622	663	523	107	127	135	308	66	71.4	105	38.1	165	13	148	11.7	4.6	5.6	133	134.4	45.1	13.6	17.4	24.4	19.1	9.5	30			
Lu	114	114	123	90.1	22.6	25.6	28.1	55.9	14.8	11.8	15.6	5.9	22.6	16.3	20.3	1.72	1.0	0.9	18.3	18.6	6.9	1.79	2.3	3.3	2.35	1.4	3.9			
Hf	8063	10195	8319	9785	15478	12690	14959	11872	12219	76.8	24.6	25.1	24.9	20.4	26.8	42.0	4.0	35.2	b.d.l.	b.d.l.	b.d.l.	b.d.l.	b.d.l.	b.d.l.	b.d.l.	b.d.l.	b.d.l.			
Ta	6.99	7.4	6.4	1.2	0.5	0.6	0.8	1.1	0.5	124	38.3	83.1	62.9	51	52.5	180	83.8	39.4	b.d.l.	b.d.l.	b.d.l.	b.d.l.	b.d.l.	b.d.l.	b.d.l.	b.d.l.	b.d.l.			
Pb	339	209	286	53.7	7.5	9.5	16.9	35.4	4.3	50	10.7	1.6	6.6	7.2	43.2	44.6	9.3	49.5	8.7	8.5	3.3	35.7	8.3	10.1	7.46	2.8	4.5			
Th	7090	10189	10261	3118	221	619	334	1028	113	643	235	317	36.3	162	332	41.6	136	60.6	219	203	34.9	99.6	42.2	82.3	50.2	26.1	75.7			
U	6500	7544	5785	3160	1340	1392	1333	2199	1247	403	28	94	47.4	124	279	81.2	46.7	114	154	119	49.4	19.8	17.4	38.6	24.9	25.8	55.9			
ΣREE	2217	2320	2241	2358	755	880	1473	1098	365	3925	3376	3363	5347	3255	4721	859	709	454	3835	4188	1634	1811	2568	3285	1833	1684	3269			
Ce _N /Yb _N	0.15	0.14	0.13	0.06	0.26	0.25	0.56	0.08	0.14	5.15	2.59	8.21	1.73	1.72	1.87	5.33	18.38	6.59	1.86	2.07	2.52	10.04	12.46	11.08	6.69	17.08	8.29			
Sm _N /Yb _N	0.10	0.07	0.06	0.46	0.85	0.83	1.23	0.17	0.75	3.72	2.66	7.23	4.29	3.51	4.03	6.09	5.73	5.95	2.80	3.16	3.34	15.38	14.91	14.60	11.12	12.70	11.77			
Eu _N /Eu _N *	0.46	0.53	0.71	0.32	0.47	0.42	0.52	0.55	0.4	0.98	1.14	1.65	0.48	0.74	0.51	5.29	5.16	5.74	0.26	0.28	0.57	0.25	0.29	0.26	0.26	0.51	0.33			

b.d.l.: below detection limits

Table 4 Whole-rock major (wt%) and trace element (ppm) composition together with Sr-Nd isotopic geochemistry of syenites

Variety	Central	Central	Marginal	Marginal	Nodule	Nodule
SiO ₂	64.03	61.74	62.24	62.59	60.85	62
TiO ₂	0.26	0.58	0.6	0.79	0.82	0.75
Al ₂ O ₃	17.65	17.13	17.02	17.22	16.71	17.13
FeO _{tot}	0.9	1.69	4.06	2.88	5.07	3.53
MgO	0.06	0.17	0.26	0.33	0.47	0.31
CaO	0.13	0.61	1.16	0.98	1.62	1.07
MnO	0.01	0.04	0.05	0.04	0.07	0.05
Na ₂ O	1.74	1.65	1.7	1.59	1.61	1.64
K ₂ O	12.7	12.16	11.53	12.03	11.31	11.82
P ₂ O ₅	0.05	0.03	0.06	0.06	0.05	0.08
LOI	0.8	0.9	0.7	0.6	0.6	0.8
Total	98.65	97.11	99.76	99.77	99.62	99.68
Sr	502	507	463	541	465	468.4
Rb	591	466	549	591	554	535.8
Ba	3051	3624	3208	6112	4190	4536
Cs	5.8	3.6	4.4	5.9	4.7	4.8
Ga	13.8	11.4	15.3	14.5	18.8	13.7
Th	312	698	22.5	85.3	53.4	43.4
U	147	330	12.8	6.4	17.8	19.9
Ta	1	1.4	1.1	2.3	2.4	2.3
Nb	9.1	17.9	25.3	25	26.9	24.1
Zr	8408	19266	674	479	1551	1412
Hf	191	434	14.9	12.4	37.8	35.2
Y	67.1	119	18.8	11	31.9	19.3
Pb	40.3	37	9.9	7.5	7.3	
Co	1.1	1.7	3.2	2.4	5	3.4
Sc	6	13	15	17	26	18
Ni	1.5	0.7	1.1	0.3	1.1	
Cr	5.4	4.5	4.3	4.8	3.1	
V	b.d.l.	b.d.l.	b.d.l.	1	1	
Zn	32	9	18	10	21	
Cu	14.7	2.3	41.3	12.5	12.6	
La	18.2	35.2	7.1	8.7	17.3	9.8
Ce	47.8	90.3	24.2	30.3	64.8	43.1
Pr	9.15	11.1	4.48	5.65	12.34	7.25
Nd	45.5	46.7	24.3	29.4	66	37.7
Sm	12.07	5.05	7.26	8.49	20.05	10.91
Eu	2.91	2.94	1.52	2.02	2.74	2.37
Gd	9.1	8.94	4.79	4.89	12.38	6.35
Tb	1.2	1.6	0.63	0.58	1.54	0.85
Dy	7.55	12.78	3.61	2.7	7.34	4.11
Ho	1.86	3.73	0.69	0.44	1.15	0.68
Er	7.57	15.78	2.02	1.13	3.3	1.87
Tm	1.41	2.96	0.33	0.16	0.44	0.3
Yb	11.2	24.0	2.23	0.9	2.63	2.05
Lu	2.15	4.55	0.35	0.15	0.41	0.31
ΣREE	177	270	84	96	212	128
Ce _N /Yb _N	1.14	0.99	2.85	8.84	6.47	5.52
Eu _N /Eu _N *	0.85	1.00	0.79	0.96	0.53	0.87
⁸⁷ Sr/ ⁸⁶ Sr	0.72793		0.72795			
⁸⁷ Sr/ ⁸⁶ Sr ₃₃₅	0.71166		0.71156			
¹⁴³ Nd/ ¹⁴⁴ Nd	0.51216		0.51222			
¹⁴³ Nd/ ¹⁴⁴ Nd ₃₃₅	0.51181		0.511832			
εNd ₃₃₅	-7.8		-7.3			

LOI: loss on ignition; b.d.l.: below detection limits; empty entries: not determined; FeO_{tot} represents total iron oxide content
 Sr-Nd isotope data recalculated for the U-Pb zircon age of 335 Ma determined for the ultrapotassic Třebíč pluton (Schaltegger et al., 2021; see Section 4.5. for details)

Table 5 Results of U-Pb geochronological dating of apatite

Grain	Atomic ratios				Concentrations				Apparent Ages (Ma)	Error corr.			
	$^{238}\text{U}/^{206}\text{Pb}$	Error 2 σ (%)	$^{207}\text{Pb}/^{206}\text{Pb}$	Error 2 σ (%)	$^{207}\text{Pb}/^{235}\text{U}$	Error 2 σ (%)	$^{206}\text{Pb}/^{238}\text{U}$	Error 2 σ (%)			U (ppm)	Th (ppm)	Sm (ppm)
1	13.509	0.369	0.290	0.023	2.965	0.205	0.074	0.0031	60.9	97.9	482	337.2	0.07
2	15.942	0.644	0.278	0.022	2.409	0.169	0.063	0.0032	71.7	108	1123	291.8	0.15
3	10.505	0.434	0.417	0.035	5.470	0.422	0.095	0.0049	27.5	38.2	264	346.0	0.20
4	8.128	0.301	0.509	0.039	8.635	0.567	0.123	0.0060	33.4	33.7	194	364.5	0.14
5	12.422	0.458	0.390	0.031	4.325	0.315	0.081	0.0039	4.7	5.7	35.2	309.1	0.18
6	15.854	0.487	0.220	0.015	1.917	0.117	0.063	0.0028	122	227	572	319.7	0.14
7	11.205	0.353	0.358	0.028	4.407	0.302	0.089	0.0040	8.7	14.7	56.2	362.1	0.12
8	11.220	0.518	0.369	0.028	4.539	0.282	0.089	0.0050	33.4	43.8	276	354.5	0.17
9	16.210	0.510	0.263	0.022	2.235	0.165	0.062	0.0028	83.8	151	565	294.1	0.11
10	15.390	0.552	0.241	0.018	2.161	0.140	0.065	0.0031	121	242	510	319.5	0.10
11	16.248	0.676	0.212	0.015	1.801	0.116	0.062	0.0032	21.9	71	121	315.7	0.23
12	12.150	0.590	0.334	0.028	3.788	0.240	0.082	0.0048	37.5	64.1	265	348.8	0.02
13	10.901	0.441	0.439	0.035	5.557	0.374	0.092	0.0047	26.7	33.3	265	318.9	0.12
14	13.187	0.416	0.324	0.024	3.387	0.218	0.076	0.0034	60.7	66.2	281	327.1	0.08
15	10.876	0.343	0.396	0.030	5.025	0.329	0.092	0.0041	50.2	72.2	235	347.8	0.07
16	14.924	0.580	0.300	0.024	2.768	0.199	0.067	0.0034	85.9	155	632	301.3	0.15
17	13.813	0.522	0.270	0.020	2.691	0.177	0.072	0.0036	79.5	151	528	340.6	0.17
18	16.876	0.495	0.178	0.013	1.456	0.097	0.059	0.0026	157	303	910	318.6	0.16
19	14.734	0.545	0.238	0.020	2.231	0.163	0.068	0.0033	73.8	78.1	247	334.9	0.10
20	16.348	0.785	0.214	0.016	1.806	0.129	0.061	0.0035	10.9	15.8	58.2	312.9	0.38
21	13.971	0.611	0.274	0.022	2.709	0.197	0.072	0.0039	8.8	82.1	269	334.4	0.26
22	14.397	0.574	0.291	0.022	2.790	0.177	0.069	0.0035	16.1	121	403	316.3	0.16
23	12.644	1.073	0.324	0.029	3.536	0.293	0.079	0.0071	9.5	13.9	73.9	340.7	0.47
24	11.529	0.533	0.357	0.034	4.266	0.359	0.087	0.0048	5.3	8.4	120	353.0	0.11
25	9.342	0.405	0.446	0.035	6.584	0.435	0.107	0.0051	1.9	38.3	321	365.9	0.16
26	11.186	0.650	0.365	0.044	4.496	0.490	0.089	0.0056	16.9	37.7	100	358.6	0.12

Table 6

Sample (run #)	J	$\pm 1s$	$^{36}\text{Ar}_{\text{atm}}/^{39}\text{Ar}_{\text{K}}$	$\pm 1s$	$^{37}\text{Ar}_{\text{Ca}}/^{39}\text{Ar}_{\text{K}}$	$\pm 1s$	$^{38}\text{Ar}_{\text{Cl}}/^{39}\text{Ar}_{\text{K}}$	$\pm 1s$	% $^{40}\text{Ar}^*$	$^{40}\text{Ar}^*/^{39}\text{Ar}_{\text{K}}$	$\pm 1s$	TGA (Ma)	$\pm 1s$	PA (Ma)	$\pm 1s$	MSWD	n/N
Bt 3GN (N317.MS3)	0.002709	0.00002885	0.001336	0.0002121	0.0009265	0.02023	-0.000619	0.0001868	99.43	68.67	0.1109	307.8	3.048	332.1	0.65692418	1.73890745	18/62
Bt 2AM (N318.MS3)	0.002706	0.00002882	-0.0002706	0.0001634	0.0004341	0.01413	-0.0009627	0.0001257	100.1	74.35	0.09118	330.7	3.239	331.4	0.6422102	1.7135574	28/98
Amp 4NL (N319.MS3)	0.002708	0.00002883	0.018	0.0003434	-0.003677	0.03014	0.001629	0.0002802	92.07	61.78	0.1609	279	2.834	NA		NA	NA
Amp 4NL (N320.MS3)	0.002708	0.00002883	-0.00001488	0.0003362	0.3696	0.05169	0.01451	0.0003289	100	74.85	0.1755	332.9	3.315	329.4	0.65618299	1.83	33/74

J: irradiation factor from co-irradiated flux monitor FC sanidine (28.305 ± 0.036 Ma; Renne et al. 2010)

% $^{40}\text{Ar}^*$: % of radiogenic argon

TGA: total gas age

PA: plateau age integrated over selected, contiguous steps

MSWD: mean squared weighted deviation of plateau steps about the corresponding PA

n/N: number of steps included in PA over total number of steps

Decla

The authors declare that they have no known competing financial interests or personal relationships that could have appeared to influence the work reported in this paper.

The authors declare the following financial interests/personal relationships which may be considered as potential competing interests:

Journal Pre-proof

Melting of phlogopite-veined mantle produced alkali-rich syenites (K_2O 11.3–12.7 wt%)

HFSE enrichment (e.g. ZrO_2 0.06–2.60 wt%) caused by low-degree partial melting

Rapid exhumation of the Variscan orogenic root recorded by $^{40}\text{Ar}/^{39}\text{Ar}$ ages (~330 Ma)

Journal Pre-proof